Published in final edited form as:
J Struct Biol. 2013 March ; 181(3): 207–222. doi:10.1016/j.jsb.2012.12.005.

Structural analysis of reactionary dentin formed in response to polymicrobial invasion

Nattida Charadram[a,b,*], **Christine Austin**[a,c], **Patrick Trimby**[d], **Mary Simonian**[a], **Michael V. Swain**[b], and **Neil Hunter**[a,b]

[a]Institute of Dental Research, Westmead Millennium Institute and Westmead Centre for Oral Health, Westmead, Sydney, New South Wales, Australia

[b]Faculty of Dentistry, University of Sydney, Sydney, New South Wales, Australia

[c]Elemental Bio-imaging Facility, Department of Chemistry and Forensic Science, University of Technology Sydney, New South Wales, Australia

[d]Australian Centre For Microscopy & Microanalysis, University of Sydney, Sydney, New South Wales, Australia

Abstract

In response to microbial invasion of dentin odontoblasts secrete an altered calcified matrix termed reactionary dentin (Rd). 3D reconstruction of focused-ion-beam scanning electron microscopy (FIB-SEM) image slices revealed helical tubular structures in Rd that contrasted with regular cylindrical tubules characteristic of dentin from healthy teeth and affected so-called physiological dentin (Pd) lying exterior to Rd. This helical structure in Rd provided effective constriction of tubule lumen diameter that formed a barrier to bacterial advance towards the dental pulp. SEM of resin cast preparations revealed altered extension of odontoblast processes through Rd. The distribution of key mineral elements was studied by combination of 3D reconstruction of focused-ion-beam based X-ray microanalysis (FIB-EDS), laser ablation-inductively coupled plasma-mass spectrometry (LA-ICP-MS) and diffuse reflectance infrared Fourier transform spectroscopy (DRIFTS). There was a marked redistribution of calcium and phosphorous in Rd together with an increase of diffusely deposited magnesium compatible with the mineral deposition phase of synthesis of this altered matrix. Changes in tubule structure and mineral content characteristic of Rd are consistent with reduced hardness and lower elastic modulus reported for this matrix. Findings provide insight into the unique structure of Rd synthesised as a primary response to infection.

Keywords

reactionary dentin; caries; helical tubule; 3D reconstruction; FIB

Corresponding authors: Dr. Nattida Charadram, DDS. (Hons), Institute of Dental Research, Level 2 Westmead Centre for Oral Health, Westmead Hospital, Sydney NSW, 2145 Phone(work) + 61-2-9845-8767, Fax(work) + 61-2-9845-7599 ncha1431@uni.sydney.edu.au.

Conflict of interest: All the authors state that they have no conflicts of interest.

Supplemental data: There are supplemental data included with submission.

1. Introduction

Dentin comprises bone-like materials consisting of an organic scaffold, mainly collagen, that contributes to the deposition of orientated hydroxyapatite nano-crystals [$Ca_{10}(PO_4)_6(OH)_2$] (Boskey, 2007; Pasteris et al., 2008). As a living tissue, dentin presents various structural gradations regulated by neurosensory odontoblasts (Farahani et al., 2011) through microscopic channels, dentinal tubules, arising from dental pulp and extending through dentin to the outer covering of enamel (tooth crown) or cementum (tooth root). Odontoblast processes extend through these permeable tubules that contain mineral-rich fluid. In human teeth, a highly mineralised collar encompassing each odontoblastic process, is present. This matrix, termed peritubular dentin, differs in structure from the surrounding collagen-rich inter-tubular dentin (Gotliv and Veis, 2007).

Dentinogenesis is a dynamic process that occurs throughout life and is regulated by external stimuli. The term physiological dentin (Pd) defines primary and secondary dentin deposited either before or after tooth root formation, respectively. This form of dentin is characterized by the regular distribution of uniformly circular tubules, that can be observed in both healthy and carious teeth. However, structural properties and chemical composition of Pd affected by the carious process are different from Pd observed in healthy teeth. Accordingly, affected dentin is signified as APd in the present study. During the protracted carious process affecting human teeth, organic acids produced by fermentative bacteria demineralise the peritubular dentin to extend tubule diameter and facilitate penetration of diverse bacterial species through the dentinal tubules (Charadram et al., 2012). This threat is sensed by the processes of the odontoblasts, possibly through activation of Toll-like receptors (Charadram et al., 2012; Jiang et al., 2006). The adaptive response of odontoblasts to polymicrobial invasion of dentin is reflected in marked changes in expression of genes that regulate deposition of calcified matrix (Charadram et al., 2012). The resulting matrix deposited on the pulpal aspect in the region of microbial invasion is termed reactionary dentin (Rd). A characteristic feature of Rd is the presence of fewer tubules that typically display apparent constrictions when viewed in semi-thin sections (Charadram et al., 2012; Farahani et al., 2010). This structure is proposed to limit bacterial advance and therefore to protect the dental pulp from infection (Farahani et al., 2010). Despite significant variation from the highly organized symmetrical structure of Pd, Rd is characterized by an ordered pattern for both collagen framework and key proteins involved in biomineralisation (Charadram et al., 2012).

The biomineral components of dentin matrices also contribute characteristic physical and biochemical properties required for the functionality of the tissue (Addadi et al., 2003; Currey, 1999; Pasteris et al., 2008; Weiner and Wagner, 1998). Biominerals within different dentinal matrices demonstrate contrasting crystal size, concentration of hydroxyl anion, phosphate and carbonate (Elliott, 2002; Glimcher, 2006). Biological apatites incorporate many elements, for instance, calcium, phosphorus, magnesium, zinc and carbon, some at ppm levels. These variations along with mineral volume fraction and collagen organisation, affect material properties including solubility, toughness, ultimate strength and stiffness (Currey, 1999; Currey, 2004). Dentin requires an optimal mix of hardness, elasticity and fluid permeability to support mastication and prevent tooth fracture. During remodelling of mineralised tissue, the cells laying down new collagen-mineral composite materials are influenced by environmental feedback (Clarke, 2008; Currey, 1999) to achieve harmony of architecture and function. In response to external stimuli such as microbial invasion in caries, the newly deposited dentin reflects the altered secretory pattern of responding odontoblasts.

Detailed knowledge of the structure of Rd is crucial for interpretation of the adaptive changes that both minimize bacterial invasion and also support the remaining tooth structure against forces of mastication. Therefore, the purpose of this study was to map the structure of Rd, including the distribution of the major mineral components. Technologies including high resolution field emission gun scanning electron microscopy (FEG-SEM), resin-cast technique for FEG-SEM, transmission electron microscopy (TEM), laser ablation-inductively coupled plasma-mass spectrometry (LA-ICP-MS), diffuse reflectance infrared Fourier transform spectroscopy (DRIFTS), focused-ion-beam scanning electron microscopy (FIB-SEM) and focused-ion-beam based X-ray microanalysis (FIB-EDS) were employed for both structural and elemental analysis.

Reported findings provide insight into the structure of Rd as a key component of the defensive strategy of the neurosensory apparatus of dental pulp to encroaching infection. Characterization of the distinguishing features relating to the structure and mineral composition of Rd provides a basis for future biomimetic tissue engineering to protect the vitality of dental pulp tissue and enhance remineralisation of affected dentin matrix.

2. Materials and Methods

Healthy non-carious (n=20) and carious (n=20) permanent molar teeth were collected from healthy patients aged 20 to 35 years who attended the dental clinics at the Westmead Centre for Oral Health, Westmead Hospital, New South Wales, Australia. Teeth used for this study were restoration-free without any sign of attrition, abrasion and erosion. The requirement for the carious lesion was for coronal caries with extensions of not more than two thirds of the depth of dentin. This study was approved by the Ethics committee of Sydney West Area Health Service. The purpose and nature of the research project were explained to patients in writing and consent form was signed.

2.1 Dentinal structure investigated under FEG-SEM

2.1.1 Longitudinal section—Samples (n=3) were processed as described previously (Charadram et al., 2012). Briefly, the tooth was split longitudinally and pre-fixed in 4% paraformaldehyde solution at 4°C for 12 h, then demineralised in 10% citric acid for 2 min. Samples were incubated in 1 mg/mL TPCK-treated Trypsin (Sigma-Aldrich; St Louis, MO, USA) in 0.2M NH_4HCO_3 at 37°C for 48 h. Samples were post-fixed in 2.5% glutaraldehyde in 0.1M cacodylate buffer at pH 7.2 for 4 h and rinsed with 0.1M cacodylate buffer at pH 7.2 for 1 h. After dehydration in a graded ethanol series (30%, 50%, 70%, 90%, 95% and 3 changes of 100%), samples were dried using hexamethyl disilazane (Sigma-Aldrich; St Louis, MO, USA) then coated with gold/palladium (Emitech K550x; UK). Observations were performed using high resolution FEG-SEM (Ultra Plus; Carl Zeiss, Germany). Images were obtained using a secondary electron detector at an accelerating voltage of 10.00 kV.

2.1.2 Cross-sectional section—Teeth (n=3) were cleaned and serial 450 μm thickness cross-sections of tooth crown were perpared using a water-cooled slow speed diamond saw sectioning machine (Isomet 5000), Buehler Ltd., Lake Bluff, IL, USA). The sections were pre-fixed and incubated in TPCK-treated Trypsin as described above without decalcification. Sections were prepared for observation under high resolution FEG-SEM (Ultra Plus; Carl Zeiss, Germany) as described above. Images were obtained using a secondary electron detector at an accelerating voltage of 10.00 kV.

The number and the distribution pattern of the un-demineralised cross-sections of dentinal tubules in Rd were analysed and compared to affected tubular dentin in the carious sample and to dentin in the healthy sample using FEG-SEM. For analysis, nine random regions of interest (ROI) per sample were selected by placing the same size pixel spot onto the middle

of the dentinal tubule presented in each area and converting this to a binary image. The density of dentinal tubules in each area was analysed and presented as percentage area of the number of dentinal tubules occupying the area in each dentin group using a measure analysis tool (Image J version 1.41o; National Institutes of Health).

The distribution pattern of dentinal tubules was analysed using the fractal count box tool (Image J version 1.41o; National Institutes of Health). The calculation of fractal count box is based on counting of the number of boxes (*y* axis) with the selected side length (*x* axis). The fractal dimension (*D*) is calculated from the slope of the best power-law fit. The *D* value represents the degree of order of the complex architecture; a high *D* value reflects a highly ordered distribution pattern while a chaotic structure results in a lower *D* value.

2.2 Resin-cast of dentinal structure investigated under FEG-SEM

The rendered organic structures within dentin, mostly the network of odontoblastic processes, are preserved by the infiltration of resin. Subsequent selective dissolution of the tissue provides a 3D cast model of the network of odontoblastic processes.

The resin-cast technique was performed by an adaptation and modification of a technique described previously (Martin et al., 1978). Briefly, the teeth (n=3) were cleaned and serial 250 μm (thick) longitudinal sections of tooth crown were cut. Sections were prefixed in 4% paraformaldehyde solution at 4°C for 12 h. Slices were dehydrated, embedded in glycol methacrylate resin (Technovit 8100; TAAB laboratory), and the surface polished using 400 and 1200 grit abrasive paper. The surface of ground sections was acid etched with 37% phosphoric acid for 10 s and washed in distilled water for 2 min, repeated 5 times. The samples were then immersed in 5% sodium hypochlorite for 5 min and washed in distilled water for 2 min, repeated 5 times. The samples were coated with gold/palladium (Emitech K550x; UK). Observations were performed using high resolution FEG-SEM (Ultra Plus; Carl Zeiss, Germany). Images were obtained using a secondary electron detector at 10.00 kV acceleration voltage.

2.3 Dentinal elemental analysis using LA-ICP-MS

Quantitative analysis of trace element components in dentin contributes complementary information on the biomineralisation of dentinogenesis and the change of dentin components in response to the carious process.

2.3.1 Sample preparation—Teeth (n=6) were cleaned and serial 350 μm thickness longitudinal sections of tooth crown were prepared. A commercial hot mounting resin (ClaroFast; Struers, Denmark) was used for embedding in a mounting press (CitoPress-1; Struers, Denmark) according to the manufacturer's protocol. The mounted sample was ground and polished to obtain a smooth and flat surface using 1 and 0.3 μm diamond paste (DP-Paste M; Struers, Denmark) on a soft cloth rotating wheel.

2.3.2 Laser ablation-inductively coupled plasma-mass spectrometry—A New Wave Research UP-213 system (Kennelec Technologies, Australia) with a Nd:YAG laser operating at 213 nm wavelength and nanosecond pulse width, was connected to an Agilent Technologies 7500cx ICP-MS (Agilent Technologies, Australia) with Tygon® tubing (i.d. 3 mm). The laser system was equipped with a Large Format Cell (LFC) and the ICP-MS with cs lenses for enhanced sensitivity.

The system was tuned daily using National Institute of Standards and Technology (NIST) Standard Reference Material (SRM) 612 Trace elements in glass for low polyatomic oxide

interference (Th+/ThO+ < 0.3 %) and high sensitivity. Optimized operating conditions for the LA-ICP-MS system are presented in Appendix A.

Sets of 7 spots were placed in different regions of the tooth; Physiological dentin (Pd), Reactionary dentin (Rd) and Pre-dentin (Pre) (Figure 5A and B). Pre-ablation was performed on each spot under the following conditions: 80 μm spot size, 5 Hz, 2 s dwell time at approximately 3.5 J cm^{-2}. A pressed pellet of certified reference material Bone Meal NIST 1486 was analysed periodically between samples under the same conditions to correct signal drift. Analyte signal intensities were background subtracted and normalised to ^{43}Ca, then an average calculated for each spot. Analytes (^{24}Mg and ^{66}Zn) were quantified using a one-point calibration curve, which is a calibration plot constructed from the blank and one standard, constructed from NIST 1486.

2.3.3 Image processing—Images of healthy and carious teeth were made by collating multiple line scans ablated across the sample sections. Each line scan produced a file in comma separated value (csv) format which was processed using Interactive Spectral Imaging Data Analysis Software (ISIDAS) (University of Technology, Sydney, Australia) into a single visualisation tool kit format (vtk) file. Each elemental map was normalised to ^{43}Ca as an internal standard. The vtk file was exported into MayaVi2 (Enthought Inc., USA) and a colour scale applied. Prior to ablation, each line scan was pre-ablated (80 μm spot size, 20 Hz, 250 μm s^{-1} at approximately 3.5 J cm^{-2}). A one-point calibration curve was constructed using NIST 1486 for quantification of minor/trace elements in the carious and healthy samples (Mg, P and Zn are certified in NIST 1486 and an indicative value is determined for C).

2.4 Dentinal structure and elements investigated under FIB-SEM and FIB-EDS

Microscopic methods that are able to image the detailed tubular network in three dimensions (3D) are best able to reveal the complexity. In this study, focused-ion-beam scanning electron microscopy (FIB-SEM) linked with a focused-ion-beam based X-ray microanalysis (FIB-EDS) was used to reveal the tubular structure and the distribution of elements within healthy dentin from sound teeth, as well as affected physiological dentin (APd) and reactionary dentin (Rd) from carious teeth, in 3D.

2.4.1 Sample preparation—Teeth (n=2) were cleaned and serial 350 μm thick slices of longitudinal sections of tooth crowns were prepared. Tooth slices were polished using 400 and 1200 grit abrasive paper. The samples were coated with gold/palladium (~ 45 nm thick) (Emitech K550x; UK).

2.4.2 FIB-SEM and FIB-EDS operation—The FIB-SEM slice and view procedures were performed using automated slice and view software (Auriga CrossBeam; Carl Zeiss, Germany). The angle between the electron and ion beams was 54°. A protective Pt layer (1–2 μm) was deposited on top of the analysed surface using ion beam deposition with the standard FIB-SEM gas injection system. The FIB was operated with a Ga ion source at an accelerating voltage of 30.00 kV. The milling currents for bulk milling were 30 nA, 5 nA for polishing and the current for slice and view layers was 1 nA. Scanning electron micrographs were obtained using a secondary electron detector with an electron beam accelerating voltage of 10.00–15.00 kV. The thickness for each slice was 500 nm, with 40 slices used to reconstruct the 3D volume (to a total depth of 20 μm).

The FIB-SEM is also equipped with an energy dispersive X-ray spectroscopy (EDS) detector, enabling elemental analyses of each milled section. Automated serial sectioning coupled with X-ray mapping of each milled surface enables the reconstruction of 3D

elemental maps. Elemental maps for calcium, phosphorus, magnesium, zinc and carbon were collected from each layer using an acceleration voltage of 15.00 kV and a Si drift detector (Oxford Instruments X-Max 20 SDD). X-ray K-lines were used for all the elements, with the exception of Zn, for which the L-lines were used to increase the excitation. The combination of ion milling and EDS mapping was fully automated using Oxford Instruments INCA smart map 3D. In addition, some manual sections were milled and mapped using the EDS system. The thickness for each slice for the 3D measurements was 500 nm, with up to 40 slices in each experiment.

2.4.3 3D reconstruction and 3D surface plot—3D reconstructions for calcium, phosphorus and magnesium were performed using ImageJ 1.41o (National Institutes of Health), Adobe Photoshop CS5 (Adobe Systems Incorporated) and ImageSurfer 1.24 (University of North Carolina, Chapel Hill). Sequentially, 25 slices of 500 nm for each milling were used for FIB-EDS 3D reconstruction and sequentially 35 slices of 500 nm for each milling were used for FIB-SEM 3D reconstruction. Images were first stacked and assembled into an aligned volume referred to a marked reference point. Background elimination, contrast enhancement and image sequence compiling were performed using ImageJ 1.41o (National Institutes of Health). The 3D reconstruction and quantitative analysis of large datasets were accomplished using ImageSurfer 1.24 (University of North Carolina, Chapel Hill).

3D surface plot was used to analyse zinc and carbon as these two elements were present with intensities too low to perform 3D reconstruction. The distribution patterns of zinc and carbon were analysed using interactive 3D surface plot plugin and the Plot Profile analysis tool (ImageJ version 1.41o; National Institutes of Health).

2.5 Dentinal mineral composition analysis using DRIFTS

The calcium-rich bioapatite structure presents numerous lattice vacancies; also a variety of substitutions (Boskey, 2007) in which the Ca/P molar ratio differs from the stoichiometric hydroxyapatite ratio of 1.67 (Zipkin, 1970) cause greater solubility relative to stoichiometric apatite. Ion exchange in hydroxyapatite molecules can take place at Ca^{2+}, PO_4^{3-} and/or OH^- sites (Wright and Schwarcz, 1996). The substitution of carbonate groups at OH^- (type A substitution) or PO_4^{3-} (type B substitution) in the hydroxyapatite matrix (Wright and Schwarcz, 1996), is of interest as carbonate substitution leads to poorly crystallized apatite and increases the solubility of the apatite (LeGeros, 1983; Posner, 1969). In this study, we focused on the B-type carbonate substitution, the preferential carbonate substitution in bone and dentin. The presence of B-type carbonate substitution in the lattice increases crystal imperfection and thereby its solubility (LeGeros, 1991; Rey et al., 1989). In association with these substitution patterns, the ratio of triply degenerate PO_4^{3-} spectral splitting between 560 and 605 cm^{-1} was used as the analysis method for Crystallinity Index (CI) which indicates the degree of crystalline perfection and/ or the relative size of crystals (Blumenthal and Posner, 1972; Termine and Posner, 1966). A higher CI implies more perfect crystals and/or the presence of greater sized crystals (Shemesh, 1990; Weiner and Bar-Yosef, 1990). The analysis of CI was also evaluated in this study.

2.5.1 Sample preparation—Teeth (n=3) were cleaned and serial 350 μm thick slices of longitudinal sections of tooth crown were prepared. Dentin powders from different areas were collected using a round steel bur (Premier; USA) at low speed. Rd areas from carious dentin slices were identified and the border marked under a dissecting stereomicroscope (LeicaMZ8; Germany) prior to dissecting and grinding.

2.5.2 DRIFTS spectra collection—Pulverized dentin was mixed with ground KBr and transferred into the sample cup. The excess across the top of the cup was removed to obtain a smooth flat surface. The sample cups were loaded into a FTIR spectrometer (Magna-IR 3700; Nicolet, Waltham, MA). Pure KBr in a separate sample cup was used for background correction. Absorbance and Kubelka-Munk infrared spectra were collected between 4000 and 400 cm^{-1} using the OMNIC (Thermo Scientific) program. Resolution was set at 8 cm^{-1} and 64 scans were taken and averaged for each spectrum.

2.5.3 Data analysis—The Kubelka-Munk (KM) function converts sample concentration and scattering factor of the crushed sample particles into intensity values, providing quantitative data from DRIFTS analysis (Kortum, 1969; Smith, 1996). The KM is defined in Appendix B.

All spectral data were converted to KM units using the OMNIC (Thermo Scientific) program for Windows. Intensities of pertinent peaks from asymmetric stretching (ν_3) vibrations of the CO_3^{2-} group of B-type carbonate substitution (~ 1450 cm^{-1}) (Fleet, 2009; Landi, 2003), and ν_2 bending vibration (870 cm^{-1}) the characteristic for type B apatite (Fleet, 2009; Landi, 2003), were normalised by reference to the intensity of the ant-isymmetric ν_3 PO_4^{3-} stretching mode at ~ 1030 cm^{-1} (Greene et al., 2004) to minimize errors due to differences in sample preparation.

In this study, we defined the Kubelka-Munk Crystallinity Index (CI_{KM}) as follows:

$$CI_{KM} = (KM_{602} + KM_{563})/KM_{586}$$

where KM_x is the Kubelka-Munk absorbance at wave number x

2.6 Apatite Crystals investigated under TEM

Healthy and carious teeth were used to investigate the structure of apatite crystals; Pd and Rd samples were obtained from the same carious tooth and acted as an internal control. A tooth was cleaned and serial 450μm thickness of cross-sections of tooth crown were prepared using a water-cooled slow-speed diamond saw. Tooth slices were fixed (2.5% glutaraldehyde, 2.4% formaldehyde, 0.008% sodium azide and 2.092% MOPS buffer) for 24 hr at 4°C. After washing in MOPS, tooth slices were post-fixed in 1.0% aqueous osmium tetroxide in 0.1 M Na-cacodylate buffer, pH 7.4 for 4 hr, rinsed with distilled water and dehydrated. A commercial low viscosity resin-premix (TAAB laboratory) was used for embedding; polymerized at 70°C for 24 hr. The sample embedded in resin was cut at ~70 nm and sections were floated on distilled water before being picked up onto formvar/ pioloform coated copper slot grids. Sections were stained with 2%-uranyl acetate and lead citrate. The sections were observed under a transmission electron microscope (Philips CM-120 BioTwin; Eindhoven, Netherlands) at 100.00 kV accelerating voltage.

2.7 Statistical analysis

Statistical analysis of data was performed using SPSS statistical software (SPSS v.16; Chicago, Illinois, US). All data are presented as mean ± SD. Statistical significance was determined by comparison between carious (APd and Rd) and healthy as a control using a two-tailed Student's t test assuming equal variance. In this study, a P-value ≤ 0.05 was considered as statistically significant.

3. Results

3.1 Histological structure of reactionary dentin

Reactionary dentin is deposited over the pulp in response to caries progression (Figure 1) with an obvious boundary between Rd and affected Pd (APd). Compared to dentin of healthy teeth (Figure 2A) and APd from carious teeth (Figure 2B), reactionary dentin (Rd) (Figure 2B) contains fewer tubules evident from the transitional zone between APd and Rd (Figure 2C). Compared to APd (Figure 2D), tubular width observed in longitudinal section is less in Rd (Figure 2E). A transitional zone can be observed between APd and Rd (Figure 3AB). Comparison of the density of odontoblastic processes in APd and Rd indicates that fewer odontoblastic processes (Figure 3C-D) remain within constricted tubules in Rd (Figure 3E).

3.2 Analysis of the number and distribution pattern of dentinal tubules

Low magnification (X200) SEM images from dentin of healthy teeth (Figure 4A) and APd (Figure 4B) from carious teeth showed a high density of dentinal tubules (Figure 4D) with a high degree of order (*D* value) of tubule distribution pattern (Figure 4E). In Rd (Figure 4C), tubule density was lower (Figure 4D) and the tubule distribution pattern was less ordered (Figure 4E). Of note, the *D* values within each category, including Rd, were similar, with implication of a consistent pattern of tubule distribution for each type of dentin (Figure 4E).

3.3 Analysis of chemical elements in dentin by LA-ICP-MS

The areas analysed for elemental images and spot analyses are displayed in Figure 5. The abundance and distribution of elements involved in biomineralisation were altered in carious teeth compared to healthy teeth. [^{31}P] was significantly increased from APd underneath the carious lesion toward the pulp. However, [^{31}P] in pre-dentin was significantly different from Rd (Figure 6A and B). [^{24}Mg] was very low in APd in contrast to the intense signal closer to the pulp (Figure 6C and D). The increase of [^{66}Zn] in carious lesions and an even more intense signal in dentin close to the pulp, was observed (Figure 6E and F). Large variation in [^{12}C] in APd was observed. Nevertheless, [^{12}C] in pre-dentin was significantly different from that in Rd (Figure 6G and H).

3.4 Elemental mapping in 3D using FIB-EDS

Three dimensional reconstruction was used to map the distribution of the major mineral components including calcium, phosphorus and magnesium detected by FIB-EDS. In healthy samples, calcium and phosphorus accumulated around tubules (peritubular cuffs) but were dispersed in inter-tubular dentin (Figure 7; Healthy A-H). Magnesium was present at high intensity with similar distribution between the area around the tubules and in the inter-tubular area (Figure 7; Healthy I-L). In APd from carious samples, intra-tubular calcium plugs were observed with lower intensity of signal in the peritubular cuff dentin (Figure 7; APd A-D). Signal pattern for phosphorus was intense adjacent to the tubules but dispersed in the inter-tubular region (Figure 7; APd E-H). Of note, magnesium was depleted from this area (Figure 7; APd I-L). In Rd all the elements presented similar distribution profiles for both peritubular and inter-tubular dentin. The same intensity was also noted in areas lacking dentinal tubules. However, phosphorus and magnesium signals were more intense compared to healthy dentin and APd (Figure 7; Rd A-L).

A 3D interactive surface plot was constructed for zinc and carbon detected by FIB-EDS. In healthy dentin samples, zinc and carbon presented weak signals but peritubular accumulation of zinc was observed (Figure 8; Healthy A-F). In APd, signals from both elements increase with accumulation of zinc around the tubules (Figure 8; APd A-F). In Rd, a higher intensity of both signals compared to healthy dentin and APd was detected.

However, the distribution of zinc was similar for the region around the tubules and the inter-tubular region (Figure 8; Rd A-F).

3.5 Apatite composition and crystallinity analysed by DRIFTS

The spectra collected from every sample were characteristic of bioapatite. The antisymmetric ν_3 PO_4^{3-} stretching vibration was found at ~1030 cm^{-1} while the anti-symmetric ν_4 PO_4^{3-} bending vibration was observed at ~563 and 602 cm^{-1}, with a valley at ~586 cm^{-1}. The intensity of ν_3 CO_3^{2-} B-type (~ 1450 cm^{-1}) carbonate substitutions was recorded for every sample as well as ν_2 CO_3^{2-} at ~ 870 cm^{-1} (Figure 9A-C). The amide I band, the most sensitive for collagen secondary structure, was observed as an intense band at 1660 cm^{-1}. Compared to healthy dentin (Figure 9A) and APd (Figure 9B), Rd (Figure 9C) showed reduced B-type carbonate substitutions in both ν_3 CO_3^{2-} and $\nu_2 CO_3^{2-}$ regions (Figure 9D). In contrast to the amount of carbonate substitution, the Crystallinity Index (CI) in Rd was significantly higher compared to healthy dentin and APd (Figure 9E).

3.6 Morphology of apatite crystals investigated by TEM

Apatite mineral was identified in each source of dentin. Apatite crystals in Rd were wider but shorter compared to those observed in healthy dentin and APd (Appendix D).

3.7 Characterization of dentin structure in 3D using FIB-SEM

In healthy dentin and APd, tubules present circular lumens along the ~20 μm length analysed (Figure 10A-F). In Rd, identical analysis indicated a consistent twisting suggesting a helical tubular structure (Figure 10G-I).

4. Discussion

The aim of this study was to provide new insight into the arrangement of components of a native dentin structure deposited as a response to encroaching infection. The tenet of the investigation was to both explain the apparent barrier against microbial invasion provided by Rd and to probe the capacity of the altered matrix of Rd to provide supporting mineralised structure that compensates for the loss of upper tooth structure caused by the carious process. The main findings are displayed in Figure 11.

Odontoblasts deposit Rd in response to caries progression resulting in contraction of the dental pulp (see Appendix C). Rd is separated from APd by transitional zones. While modified, the degree of order (*D* value) of tubular distribution implies an organized pattern coinciding with a previous report from our group showing a structured pattern of the collagen framework and the uniformity of gene expression for key aspects of deposition of such a mineralised matrix (Charadram et al., 2012). This suggests a systematic plan for deposition of this modified matrix from active odontoblasts that is supported by the location of odontoblastic processes within the tortuous tubules of Rd. The presence of these open mineral-rich channels provides the capacity for odontoblasts to deposit the altered matrix of Rd in response to disruption of structure by the carious process. Significantly increased deposition of the elements related to biomineralisation, including: P, Mg and Zn in Rd, implies active mineralisation. The increase of P from dentino-enamel junction towards the coronal dentin as observed in this study also corresponds with the Fourier-Transform Infrared Micro-spectroscopy in Reflectance Mode (FTIR-RM) data reported earlier (Tesch et al., 2001). Calcium and phosphorus are the major components of hydroxyapatite crystals accumulating in peritubular dentin, which is known to be a porous mineralised structure containing a calcium-proteolipid-phospholipid-phosphate complex (Gotliv and Veis, 2007). Demineralisation of APd mobilises calcium from peritubular dentin for the formation of intra-tubular calcific plugs considered to be a first line of defence (Fusayama, 1993).

Phosphate in peritubular dentin seems not to be critically affected by the demineralisation process indicating the persistence of a phospholipid-phosphate complex within the peritubular structure of APd. The remaining phospholipid-phosphate complex found in APd suggests a capability for remineralisation in this area. In Rd, odontoblastic processes remote from relatively atubular regions apparently coordinate deposition of calcium and phosphorus into these areas as deduced by the uniformity of deposition of these elements in Rd. However, phosphorus showed slightly higher intensity in Rd compared to healthy dentin and APd, possibly related to the increase of dentin sialophosphoprotein (DSPP) and cleavage products of this molecule as nucleation sites for mineral deposition (Charadram et al., 2012).

Magnesium is a crucial element in biological systems, assisting function in many cell types as a signalling ion, both activating and mediating biochemical reactions. In mineralised tissue, magnesium binds to the surface of hydroxyapatite crystals to regulate the crystallization process and indirectly influence enzymatic functions, for instance the activation of alkaline phosphatase (Wacker and Parish, 1968a; Wacker and Parish, 1968b; Wacker and Parish, 1968c)). High intensity magnesium signal is detected in rapidly forming mineralised tissue, while the constant lower level of magnesium in mature matrices serves as a reservoir (Wiesmann et al., 1997). In this context magnesium was depleted in APd. Magnesium can be incorporated into the lattice structure of hydroxyapatite crystals and form magnesium whitlockite (Lagier and Baud, 2003). However, the magnesium concentration in teeth and bone in physiological conditions is too low to form a detectable whitlockite phase (Gotliv et al., 2006; Trautz et al., 1964). Magnesium is also found to bind onto the hydrated surface layers, providing a readily mobilised source (Neuman and Neuman, 1953; Wallach, 1988; Wallach, 1990). There are two possibilities for the depletion of magnesium in APd: invading bacteria sequester magnesium for metabolic processes; alternatively, odontoblasts mobilise and re-deploy this magnesium to serve in Rd formation. These two potentially competing processes could mediate depletion of magnesium from APd, a critical region for potential remineralisation by physiological mechanisms or therapeutic manipulations. The importance of magnesium is indicated by the finding that deficiency of magnesium reduces bone mass and increases skeletal fragility *in vivo* (Rude and Gruber, 2004; Wallach, 1988; Wallach, 1990).

Zinc and carbon, although minor components in dentin, are involved in biomineralisation (Kirsch et al., 2000). Zinc is also known to play a role in tissue degradation as shown by intense signal in carious lesions, as zinc is the essential activator of matrix metalloproteinases (Rosenblum et al., 2003; Springman et al., 1990). In newly formed mineralised matrix, such as Rd, zinc also mediates biomineralisation by regulating calcium uptake, matrix vesicle-mediated mineralisation and growth of hydroxyapatite (Kirsch et al., 2000). The intense Zn signal in Rd could also be explained by the occurrence of less soluble Zn phosphate providing the critical nuclei for subsequent precipitation of calcium phosphate. Zinc deficiencies result in abnormal cartilage development, irregular bone formation and increase in bone deformity (Bergman et al., 1970; Da Cunha Ferreira et al., 1991; Westmoreland and Hoekstra, 1969). The stronger signal for carbon detected in Rd could relate to the increase of representation of organic compounds during reactionary dentin formation (Charadram et al., 2012).

According to DRIFTs analysis, the intense band related to the organic phase, namely amide I reflecting collagen secondary structure, was observed at 1660 cm^{-1} in every sample. This is similar to other studies reporting organic phase-related bands in teeth (Leventouri et al., 2009; Magne et al., 2001). The inorganic bands reflecting B-type carbonate substitution were decreased for both ν_2 CO_3^{2-} (~ 870 cm^{-1}) and ν_3 CO_3^{2-} (~ 1450 cm^{-1}) regions in Rd. The spectral peak in ν_2 CO_3^{2-} (~ 870 cm^{-1}) is characteristic of B-type carbonate substitution in mineralised tissue (Figueiredo et al., 2012). This indicates markedly

decreased B-type substitution coinciding with the substantial amount of phosphorus detected in Rd. Significant carbonate substitutions cause distortion of hydroxyapatite structure by difference in charge, shape and size from both OH^- and PO_4^{3-} (Blumenthal et al., 1975). Reduced carbonate substitution results in less soluble and/or less defective organization of crystals and/or increase of crystal size. Reactionary dentin has higher CI with wider but shorter apatites compared to crystals obtained from APd and healthy dentin. The interaction between anionic acidic proteins and the nucleated crystal defines crystal size and shape (Addadi and Weiner, 1985; Addadi et al., 2001; Du et al., 2005). In the unique mineralisation of reactionary dentin, dense depositions of dentin sialoprotein (DSP) were detected in contrast to APd and healthy dentin (Charadram et al., 2012). Non-collagenous proteins preferentially regulate nucleation sites (Linde and Lussi, 1989) and have the capacity to interfere with or retard crystal growth (Linde and Lussi, 1989; Termine et al., 1981) by binding onto the crystal surface thus preventing further aggregations. (Linde and Lussi, 1989; Lowenstam and Weiner, 1989; Mann et al., 1988). Up-regulation of dentin sialophosphoprotein (DSPP) from odontoblasts and dense depositions of the cleaved product DSP along the collagen fibrils are characteristic of reactionary dentin formation (Charadram et al., 2012; Farahani et al., 2010). DSP initiates mineral deposition, and presumably limits the size and number of hydroxyapatite crystals in this area. Increasing crystallinity suggests a greater proportion of crystals have larger size and/or stoichiometrically less defective lattice with fewer substitutions (Dziak and Akkus, 2008). However, infrared spectroscopy is not able to disengage the influence of crystallite size from the lattice imperfection (Farlay et al., 2010). The increased crystallinity in Rd is credibly related to reduced lattice imperfection due to fewer carbonate substitutions.

Reduction in the number of apatite crystals observed in Rd is compatible with reduced levels of calcium observed here and the report of reduced hardness for this matrix (Glimcher, 1998; Senawongse et al., 2006). Although stiffness is required for most mineralised tissues, the undesirable mechanical result of brittleness is a disadvantage. During mastication, the tooth, as a single unit, is subjected to compressive load and frictional contact. Dentin, as the major calcified matrix of the tooth, is modified to obtain the appropriate mix of stiffness and toughness to prevent fracture (Currey, 1999). While all dentin matrices display a similar structural plan, there are distinct functional attributes for each type (Zaytsev et al., 2012). Considering the loss of tooth structure in extensive caries and the compromised APd resulting from the carious process (Nishitani et al., 2005), there is a requirement for Rd to provide an appropriate deformable and resilient foundation to resist tooth fracture under high stress. This modification manifests as a lower elastic modulus reported for Rd compared to APd (Senawongse et al., 2006). The reduction of hardness and elastic modulus of Rd has been attributed to the decrease in mineral content (Senawongse et al., 2006). This was confirmed in the present study where reduction of abundance of hydroxyapatite crystals was noted for Rd compared to APd (Appendix D).

Tubular orientation and density are reported to influence mechanical properties of dentin (Kinney et al., 2003; Kinney et al., 1999; Waters, 1980). However, the mechanical properties of dentin have been attributed mostly to the matrix of inter-tubular dentin where the alignment of collagen fibrils is perpendicular to the tubular axis (Kinney et al., 2003). Instead of the circular and straight tubular structure observed for dentin from healthy teeth and also in APd, tubules in Rd displayed a helical structure for all tubules observed in this study. The helical tubular structure in Rd combined with altered organic and mineral composition of the matrix, provides a credible basis for the reduced elastic modulus of this tissue (Senawongse et al., 2006) while also impeding the invasion of bacteria (Farahani et al., 2010). The helical structure of Rd is not apparent from 2D analysis, for instance in cross-sectional or longitudinal sections of Rd observed under SEM, which is dependent on the axis of sample preparation. Also, the twisted portion of the tubule, when examined in cross-

section, has the appearance of a slit (see Figure 10G). Presumably, the helical structure reflects an altered balance of elongation of the odontoblast process and mineral deposition, resulting in a spiral configuration to accommodate the altered dynamics of mineral deposition. These constrictions potentially enhance resistance to bacterial penetration. Further investigations are required to confirm that the modified helical tubular structure of Rd contributes to the increased resistance to dynamic load exhibited by this tissue. The high resolution structural and compositional data obtained for this remarkable natural material provide a basis for biomimetic tissue engineering to replace loss of dentin caused by the carious process in order to increase compatibility and sustain the natural remineralisation process.

5. Conclusions

Findings indicate key details of the characteristics of a unique calcified matrix formed in response to carious stimulation. Attributes of this design include a barrier to microbial invasion by reducing the effective diameter and number of tubules. Also, the helical form of the tubules together with the lower mineral density of Rd are compatible with an efficient shock absorber to compensate for dynamic load caused by significant loss of upper tooth structure due to the carious lesion.

Supplementary Material

Refer to Web version on PubMed Central for supplementary material.

Acknowledgments

NC would like to thank Manish Arora, Ramin Farahani, Brian Reedy and Steve Moody for valuable technical support and discussion. Scanning electron microscopy was performed with the scientific and technical support from staff at the Australian Microscopy & Microanalysis Research Facility, at The University of Sydney. This work was supported by a grant to NH from the National Institutes of Health (R01 DEO15272-07) and to NH and MS from the Australian National Health and Medical Research Council (Grant 512524.3). NC was supported by a Naresuan University Thailand Staff Development Project scholarship.

References

Addadi L, Weiner S. Interactions between acidic proteins and crystals: stereochemical requirements in biomineralization. Proc Natl Acad Sci U S A. 1985; 82:4110–4114. [PubMed: 3858868]

Addadi L, Geva M, Weiner S. On how proteins interact with crystals and their effect on crystal formation. Z Kardiol. 2001; 90:92–98. [PubMed: 11374040]

Addadi L, Raz S, Weiner S. Taking advantage of disorder: amorphous calcium carbonate and its roles in biomineralization. Adv Mat. 2003; 15:959–970.

Bergman B, Friberg U, Lohmander S, Oberg T. Morphologic and autoradiographic observations on the effect of zinc deficiency on endochondral growth sites in the white rat. Odontol Revy. 1970; 21:379–399. [PubMed: 5276721]

Blumenthal NC, Posner AS. Effect of preparation conditions on the properties and transformation of amorphous calcium phosphate. Mat Res Bull. 1972; 7:1181–1190.

Blumenthal NC, Betts F, Posner AS. Effect of carbonate and biological macromolecules on formation and properties of hydroxyapatite. Calcif Tissue Int. 1975; 18:81–90.

Boskey A. Mineralization of bones and teeth. Elements. 2007; 3:385–391.

Charadram N, Farahani RM, Harty D, Rathsam C, Swain MV, Hunter N. Regulation of reactionary dentin formation by odontoblasts in response to polymicrobial invasion of dentin matrix. Bone. 2012; 50:265–275. [PubMed: 22079283]

Clarke B. Normal bone anatomy and physiology. Clin J Am Soc Nephro. 2008; 3:S131–S139.

Currey JD. The design of mineralised hard tissues for their mechanical functions. J Exp Biol. 1999; 202:3285–3294. [PubMed: 10562511]

Currey JD. Tensile yield in compact bone is determined by strain, post-yield behaviour by mineral content. J Biomech. 2004; 37:549–556. [PubMed: 14996567]

Da Cunha Ferreira RMC, Gonzales RJI, Marquiegui MI, Elizaga VI. Changes in the fetal tibial growth plate secondary to maternal zinc deficiency in the rat: A histological and histochemical study. Teratology. 1991; 44:441–451. [PubMed: 1962289]

Du C, Falini G, Fermani S, Abbott C, Moradian-Oldak J. Supramolecular assembly of amelogenin nanospheres into birefringent microribbons. Science. 2005; 307:1450. [PubMed: 15746422]

Dziak KL, Akkus O. Effects of polyelectrolytic peptides on the quality of mineral crystals grown in vitro. J Bone Miner Metab. 2008; 26:569–575. [PubMed: 18979156]

Elliott, JC. Calcium phosphate biominerals. In: Kohn, MJ., et al., editors. Phosphates: Geochemical, Geobiological, and Material Importance. Reviews in Mineralogy & Geochemistry. 2002. p. 427-454.

Farahani RM, Simonian MR, Hunter N. Blueprint of an ancestral neurosensory organ revealed in glial networks in human dental pulp. J Comp Neurol. 2011; 519:3306–3326. [PubMed: 21681747]

Farahani RM, Nguyen KA, Simonian MR, Hunter N. Adaptive calcified matrix response of dental pulp to bacterial invasion is associated with establishment of a network of glial fibrillary acidic protein $^{+}$/Glutamine Synthetase^{+} Cells. Am J Pathol. 2010; 177:1901–1914. [PubMed: 20802180]

Farlay D, Panczer G, Rey C, Delmas P, Boivin G. Mineral maturity and crystallinity index are distinct characteristics of bone mineral. J Bone Miner Metab. 2010; 28:433–445. [PubMed: 20091325]

Figueiredo, MM.; Gamelas, JAF.; Martins, AG. Characterization of Bone and Bone-Based Graft Materials Using FTIR Spectroscopy, Infrared Spectroscopy - Life and Biomedical Sciences. In: Theophanides, T., editor. Infrared Spectroscopy - Life and Biomedical Sciences. 2012. InTech.

Fleet ME. Infrared spectra of carbonate apatite: V2-Region bands. Biomaterials. 2009; 30:1473–1481. [PubMed: 19111895]

Fusayama, T. New concepts in the pathology and treatment of dental caries. St Louis: Ishiyaku EuroAmerica Inc; 1993.

Glimcher MJ. The nature of the mineral phase in bone: Biological and clinical implications. Metabolic bone disease Chap. 1998; 2:23–50.

Glimcher, MJ. Bone: Nature of the calcium phosphate crystals and cellular,structural, and physical chemical mechanisms in their formation. In: Sahai N, SM., editor. Medical Mineralogy and Geochemistry. Reviews in Mineralogy & Geochemistryp. 2006. p. 223-282.

Gotliv BA, Veis A. Peritubular dentin, a vertebrate apatitic mineralized tissue without collagen: role of a phospholipid-proteolipid complex. Calcif Tissue Int. 2007; 81:191–205. [PubMed: 17674072]

Gotliv BA, Robach JS, Veis A. The composition and structure of bovine peritubular dentin: Mapping by time of flight secondary ion mass spectroscopy. J Struct Biol. 2006; 156:320–333. [PubMed: 16600633]

Greene EF, Tauch S, Webb E, Amarasiriwardena D. Application of diffuse reflectance infrared Fourier transform spectroscopy (DRIFTS) for the identification of potential diagenesis and crystallinity changes in teeth. Microchemical. 2004; 76:141–149.

Jiang HW, Zhang W, Ren BP, Zeng JF, Ling JQ. Expression of toll like receptor 4 in normal human odontoblasts and dental pulp tissue. J Endod. 2006; 32:747–751. [PubMed: 16861074]

Kinney JH, Marshall SJ, Marshall GW. The mechanical properties of human dentin: a critical review and re-evaluation of the dental literature. Crit Rev Oral Biol Med. 2003; 14:13–29. [PubMed: 12764017]

Kinney JH, Balooch M, Marshall GW, Marshall SJ. A micromechanics model of the elastic properties of human dentine. Arch Oral Biol. 1999; 44:813–822. [PubMed: 10530914]

Kirsch T, Harrison G, Worch KP, Golub EE. Regulatory roles of zinc in matrix vesicle-mediated mineralization of growth plate cartilage. J Bone Miner Res. 2000; 15:261–270. [PubMed: 10703927]

Kortum, G. Reflectance Spectroscopy. Berlin: Springer; 1969.

Lagier R, Baud CA. Magnesium whitlockite, a calcium phosphate crystal of special interest in pathology. Pathol Res Pract. 2003; 199:329–335. [PubMed: 12908523]

Landi E. Carbonated hydroxyapatite as bone substitute. Journal of the European Ceramic Society. 2003; 23:329–333.

LeGeros, RZ. Ultrastructural properties of human enamel apatite. In: Lazzari, EP., editor. Handbook of Experimental Aspects of Oral Biochemistry. Boca Raton, FL: CRC Press; 1983. p. 159-179.

LeGeros, RZ. Calcium Phosphates in Oral Biology and Medicine Monographs in Oral Science. Vol. Vol. 15. New York: Karger; 1991.

Leventouri TH, Antonakos A, Kyriacou A, Venturelli R, Liarokapis E, Perdikatsis V. Crystal structure studies of human dental apatite as a function of age. Int J Biomater. 2009:698547. [PubMed: 20130802]

Linde A, Lussi A. Mineral induction by polyanionic dentin and bone proteins at a physiological ionic conditions. Connect Tissue Res. 1989; 21:197–202. [PubMed: 2605943]

Lowenstam, HA.; Weiner, S. On Bio-mineralization. New York: Oxford University Press; 1989.

Magne D, Weiss P, Bouler JM, Laboux O, Daculsi G. Study of the maturation of the organic (type I collagen) and mineral (nonstoichiometric apatite) constituents of a calcified tissue (dentin) as a function of location: a Fourier transform infrared microspectroscopic investigation. Journal of Bone and Mineral Research. 2001:16.

Mann S, Heywood BR, Ramaj S, Birchall JD. Control crystallization of CaCO3 under stearic acid monolayers. Nature. 1988; 334:692–695.

Martin DM, Hallsworth AS, Buckley T. A method for the study of internal spaces in hard tissue matrices by SEM, with special reference to dentine. J Microsc. 1978; 112:345–352. [PubMed: 347084]

Neuman WF, Neuman MW. The nature of the mineral phase of bone. Chem Rev. 1953; 53:1–45.

Nishitani Y, Yoshiyama M, Tay FR, Wadgaonkar B, Waller J, Agee K, Pashley DH. Tensile strength of mineralized/demineralized human normal and carious dentin. J Dent Res. 2005; 84:1075–1078. [PubMed: 16246945]

Pasteris JD, Wopenka B, Valsami-Jones E. Bone and tooth mineralization:Why apatite? Elements. 2008; 4:97–104.

Posner AS. Crystal chemistry of bone mineral. Physiol Rev. 1969; 49:760–791. [PubMed: 4898602]

Rey C, Collins B, Goehl T, Dickson IR, Glimcher MJ. The carbonate environment in bone mineral: a resolution-enhanced Fourier Transform Infrared Spectroscopy Study. Calcif Tissue Int. 1989; 45:157–164. [PubMed: 2505907]

Rosenblum G, Meroueh SO, Kleifeld O, Brown S, Singson SP, Fridman R, Mobashery S, Sagi I. Structural basis for potent slow binding inhibition of human matrix metalloproteinase-2 (MMP-2). J Biol Chem. 2003; 278:27009–27015. [PubMed: 12679334]

Rude RK, Gruber HE. Magnesium deficiency and osteoporosis: animal and human observations. J Nutr Biochem. 2004; 15:710–716. [PubMed: 15607643]

Senawongse P, Otsuki M, Tagami J, Mjor I. Age-related changes in hardness and modulus of elasticity of dentine. Arch Oral Biol. 2006; 51:457–463. [PubMed: 16426564]

Shemesh A. Crystallinity and diagenesis of sedimentary apatites. Geochim Cosmochim Acta. 1990; 54:2433–2438.

Smith, BC. Fourier Transform Infrared Spectroscopy. Boca Raton, FL: CRC Press; 1996.

Springman EB, Angleton EL, Birkedal HH, Van WHE. Multiple modes of activation of latent human fibroblast collagenase: evidence for the role of a Cys73 active-site zinc complex in latency and a “cysteine switch” mechanism for activation. Proc. Natl. Acad. Sci. USA. 1990; 87:364–368. [PubMed: 2153297]

Termine JD, Posner AS. Infrared analysis of rat bone: Age dependency of amorphous and crystalline mineral fractions. Science. 1966; 153:1523–1525. [PubMed: 5917783]

Termine JD, Belcourt AB, Conn KM, Klienman H. Mineral and collagenbinding protein of Fetal calf bone. J Biol Chem. 1981; 256:10403.. [PubMed: 6793579]

Tesch W, Eidelman N, Roschger P, Goldenberg F, Klaushofer K, Fratzl P. Graded microstructure and mechanical properties of human crown dentin. Calcif Tissue Int. 2001; 69:147–157. [PubMed: 11683529]

Trautz OR, Legeros RZ, Legeros JP. Effect of magnesium on various calcium phosphate. J Dent Res. 1964; 43:751..

Wacker WEC, Parish AF. Medical progress: Magnesium metabolism (concluded). New Engl J Med. 1968a; 45:772–776. [PubMed: 4867053]

Wacker WEC, Parish AF. Medical progress: Magnesium metabolism. New Engl J Med. 1968b; 45:658–663. [PubMed: 4866353]

Wacker WEC, Parish AF. Medical progress: Magnesium metabolism (continued). New Engl J Med. 1968c; 45:712–716. [PubMed: 4867051]

Wallach S. Availability of body magnesium during magnesium deficiency. Magnesium Magnesium. 1988; 7:262–270.

Wallach S. Effects of magnesium on skeletal metabolism. Magnes Trace Elem. 1990; 9:1–14. [PubMed: 2184830]

Waters NE. Some mechanical and physical properties of teeth. Symp Soc Exp Biol. 1980; 34:99–135. [PubMed: 7020144]

Weiner S, Bar-Yosef O. State of preservation of bones from prehistoric sites in the near East: A survey. J Arch Sci. 1990; 17:187–196.

Weiner S, Wagner HD. The material bone: Structure-mechanical function relations. Annual Review of Materials Science. 1998; 28:271–298.

Westmoreland N, Hoekstra WG. Pathological defects in the epiphyseal cartilage of zinc-deficient chicks. J Nutr. 1969; 98:76–82. [PubMed: 5784259]

Wiesmann HP, Tkotz T, Joos U, Zierold K, Stratmann U, Szuwart T, Plate U, Höhling HJ. Magnesium in newly formed dentin mineral of rat incisor. J Bone Miner Res. 1997; 12:380–383. [PubMed: 9076580]

Wright LE, Schwarcz HP. Infrared and isotopic evidence for diagenesis of bone apatite at Dos Pilas, Guatemala: Palaeodietary implications. J Arch Sci. 1996; 23:933–944.

Zaytsev D, Grigoriev S, Panfilov P. Deformation behavior of human dentin under uniaxial compression. Int J Biomater. 2012; 2012:854539.. [PubMed: 22315610]

Zipkin, I. The inorganic composition of bones and teeth. In: S, H., editor. Biological Calcification: Cellular and Molecular Aspects. New York: Appleton Century Crofts; 1970.

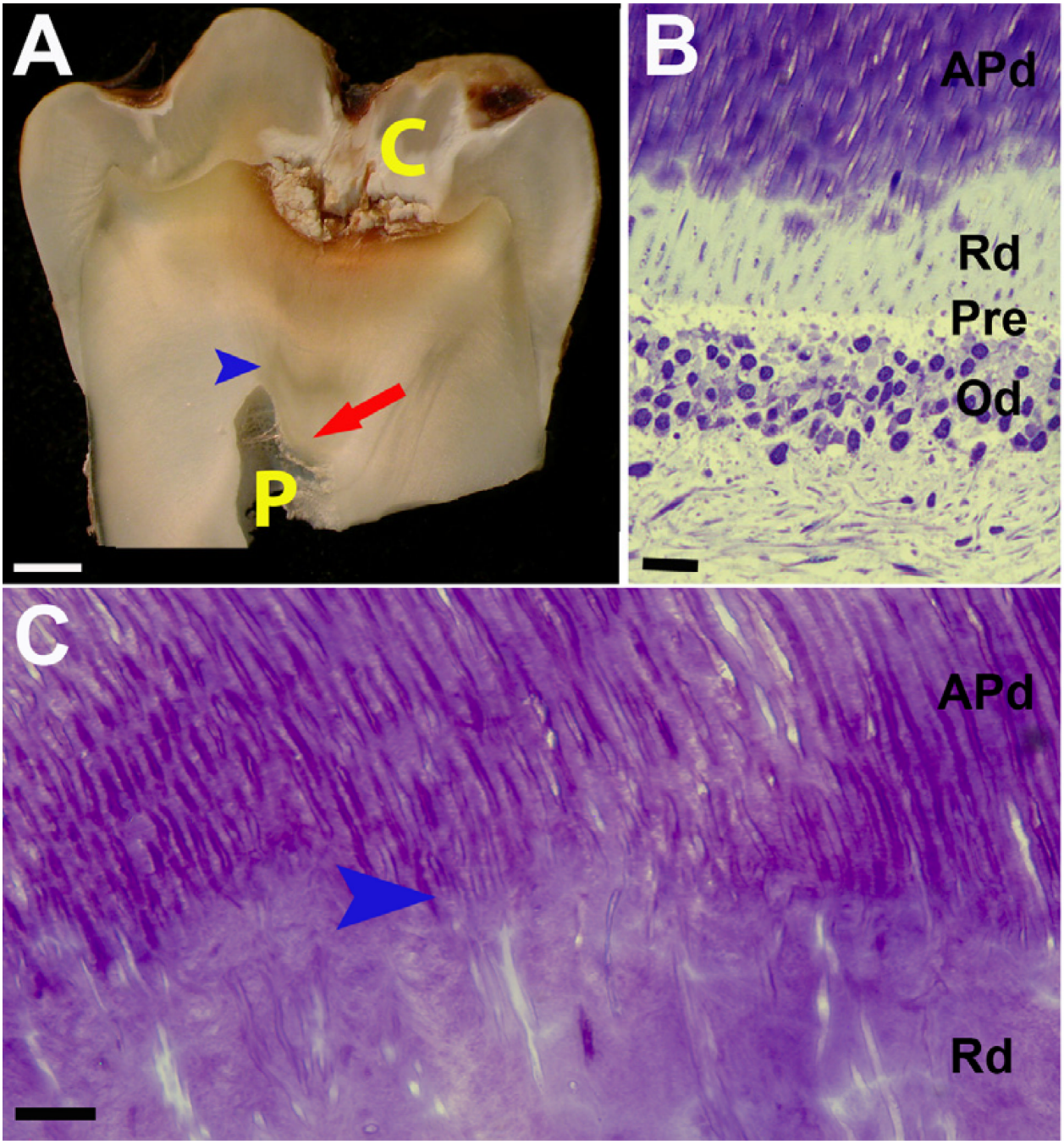

Figure 1. Representative images demonstrating the localized response of reactionary dentin (Rd) formation

(A) In this carious tooth, Rd (red arrow) is deposited beneath the carious lesion (C) and affected physiological dentin (APd) with an obvious boundary between APd and Rd (blue arrow head). The pulp (P) has been reduced by deposition of Rd. (B) Toluidine blue stain of longitudinal section from an early stage of Rd formation showing the interface between odontoblasts (Od) and dentin. The limited amount of Rd is located inferior to APd but superior to pre-dentin (Pre) and the odontoblasts (Od). Scale bar 10 μm. (C) High magnification of Toluidine blue of longitudinal section of dentin from carious tooth presents

the structure of Rd relative to APd. The varying course and wide to narrow lumen observed in Rd suggestive of spiral conformation. Scale bar 10 μm.

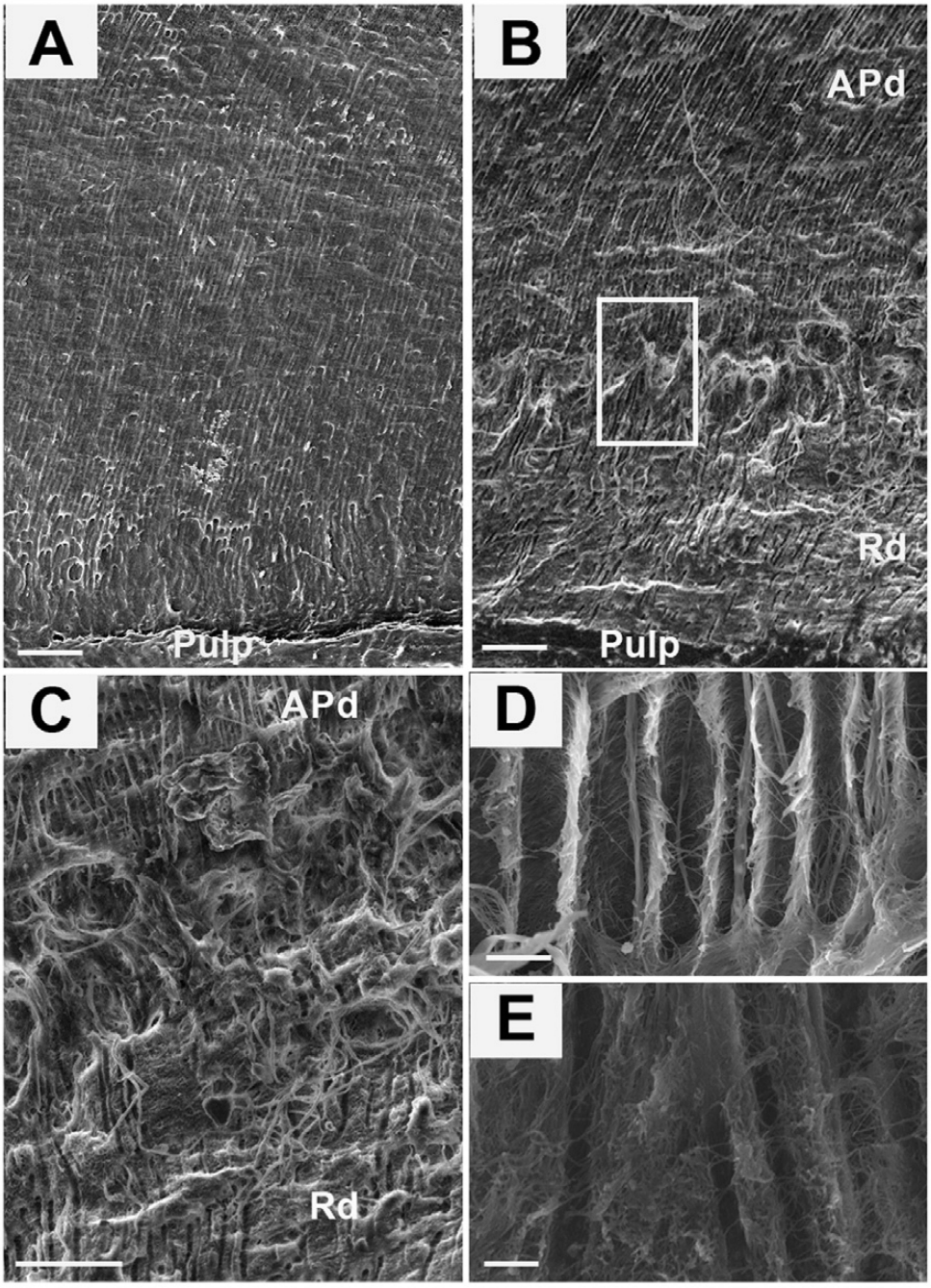

Figure 2. Scanning electron micrographs (SE detector at 10.00 kV) showing the tubular structure of healthy and carious samples

Reactionary dentin (Rd) displays fewer tubules with constrictions and irregular shapes. (A) A low magnification view (X400) of a fresh fracture of a healthy dentin sample in longitudinal section. Scale bar 20 μm. (B) A low magnification view (X400) of a carious sample reveals the different structure in the area of affected physiological dentin (APd) compared to reactionary dentin (Rd). Scale bar 20 μm. (C) A high magnification view (X1,200) of the boundary between APd and Rd of the boxed area in B. Scale bar 20 μm. (D) A high magnification view (X2,500) of the morphology of Pd. Scale bar 2 μm. (E) A high magnification view (X2,500) of the morphology of Rd. Scale bar 2 μm.

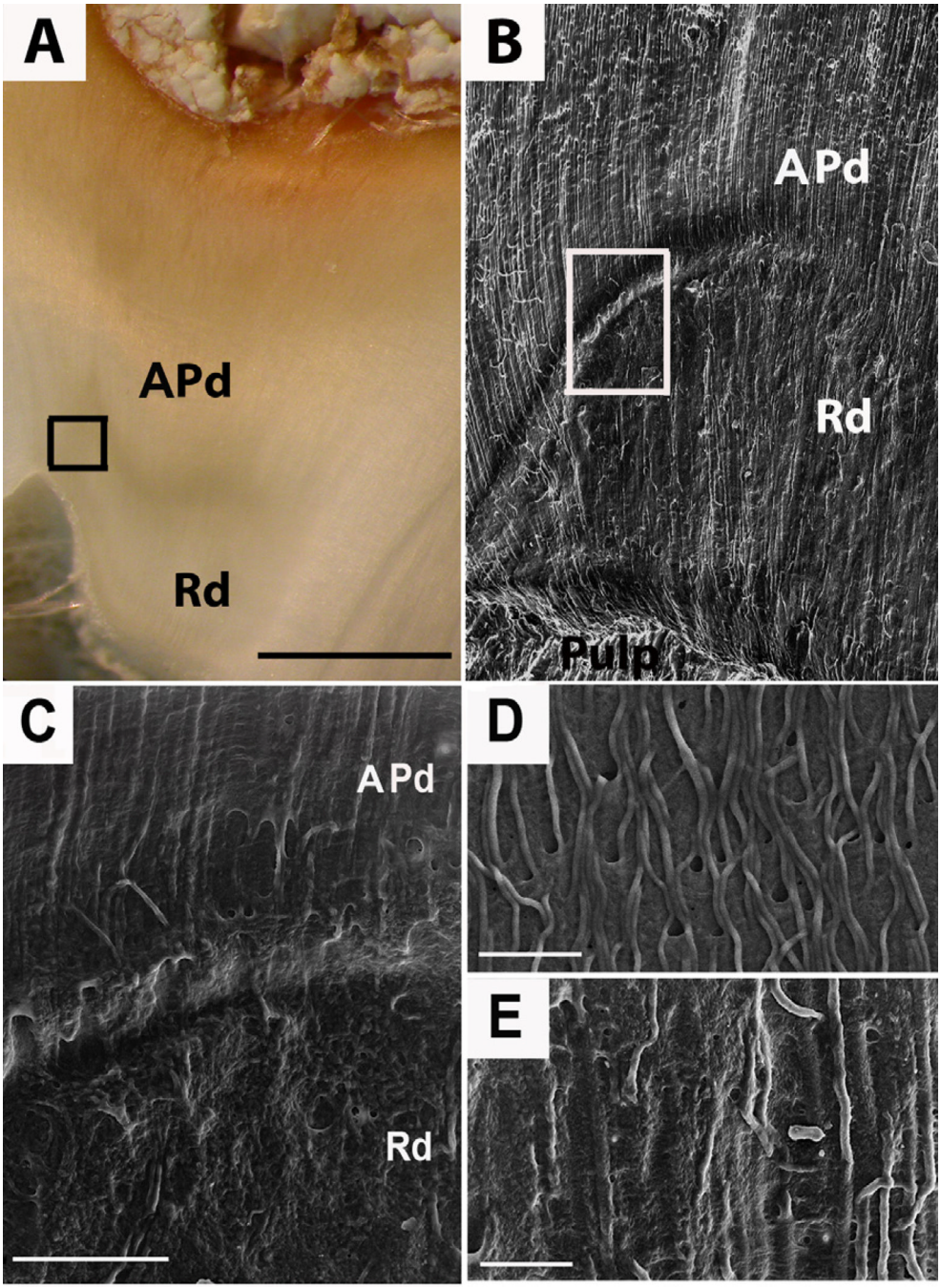

Figure 3. Resin-cast technique of carious dentin samples investigated by scanning electron microscopy (SE detector at 10.00 kV) showing the network of odontoblastic processes in dentin

Reactionary dentin (Rd) presents fewer odontoblastic processes with more irregular shape. (A) Representative image demonstrating position and boundary (boxed) between APd and Rd. Scale bar 2 mm. (B) A low magnification view (X400) of the carious sample reveals the different structure of affected physiological dentin (APd) compared to Rd; also the clear separation between APd and Rd evident by the transition zone (boxed). Scale bar 20 μm. (C) A high magnification view (X1,200) of the boundary between APd and Rd of the boxed area in B. Scale bar 20 μm. (D) A high magnification view (X1,800) of the morphology of the

odontoblastic processes in APd. Scale bar 10 μm. (E) A high magnification view (X1,800) of the morphology of the odontoblastic processes in Rd. Scale bar 10 μm.

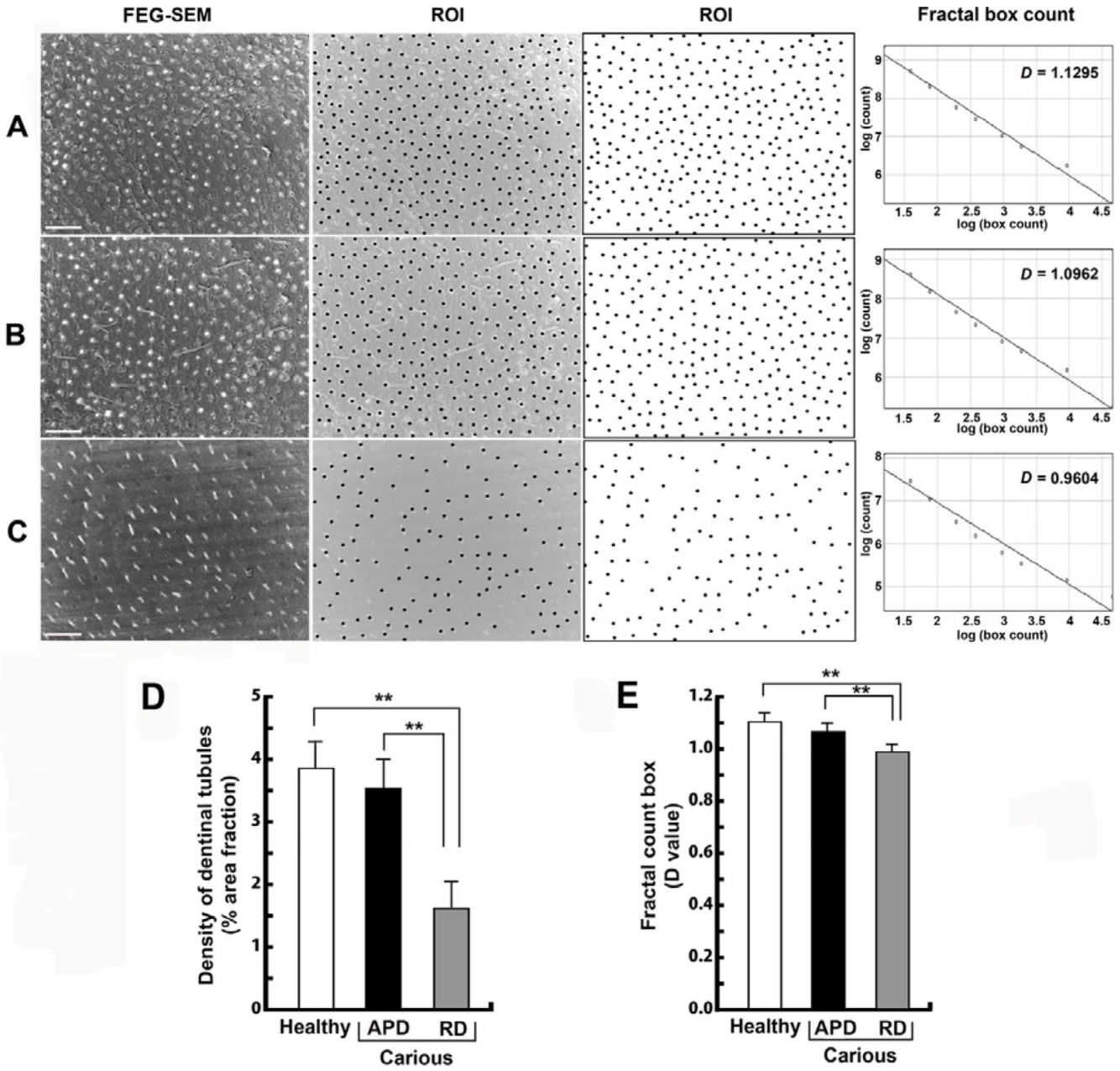

Figure 4. Representative images demonstrating the tubular distribution pattern in healthy and carious samples

Rd presents fewer numbers of tubules and with a lower degree of order of tubular distribution pattern compared to healthy dentin and APd. (A) Cross-sectional view of tubular distribution pattern in a healthy tooth. Uniformly distributed tubules are observed (first to third panel) [ROI = region of interest]. Scale bar 20 μm. Findings were confirmed by analysis of fractal count box (fourth panel). (B) Tubular distribution pattern of APd from a carious tooth. Uniformly distributed tubules are also observed in APd (first to third panel). Scale bar 20 μm. (C) Tubular distribution pattern of Rd from carious tooth indicates a lower degree of order of tubular distribution pattern (first to third panel). Scale bar 20 μm. (D) Bar chart demonstrating the percentage area fraction of the density of dentinal tubules in each area (n=27 fields from 3 teeth). (E) Bar chart representing degree of order in each dentin

area (n=27 fields from 3 teeth). The data for tubular analysis are expressed as mean values ± SD. ** $p < 0.02$.

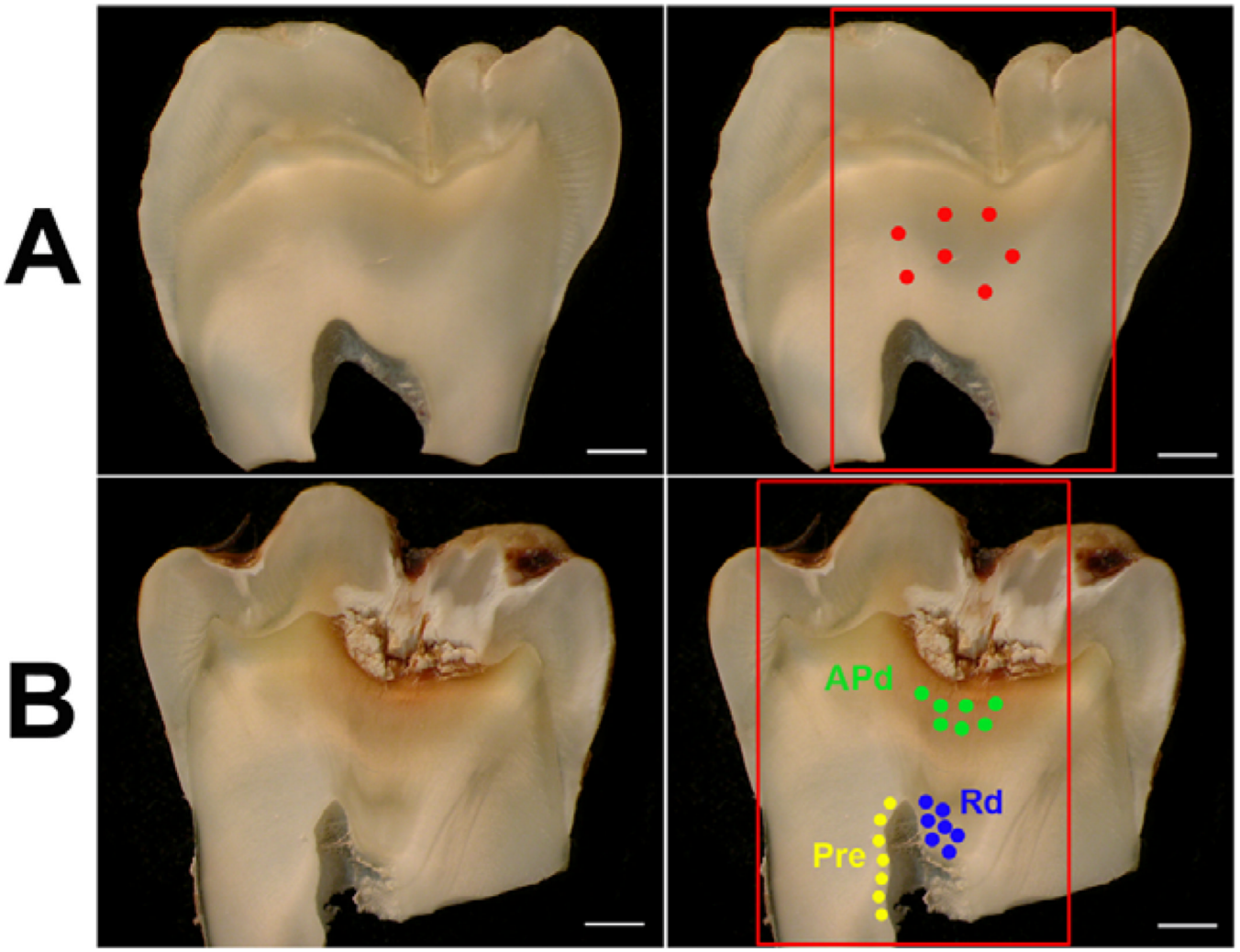

Figure 5. Representative images demonstrating the area analysed by LA-ICP-MS in both healthy and carious samples

(A) Longitudinal section of healthy sample (first and second panels). The area in the red box demonstrates the area analysed for elemental images and the seven red spots indicate the area analysed for spot analysis (second panels). Scale bar 2 mm. (B) Longitudinal section of carious sample (first and second panels). The area in the red box shows the area analysed for elemental imaging. The green spots show the areas of spot analysis of affected physiological dentin (APd), the blue spots demonstrate the area of spot analysis of reactionary dentin (Rd) and the yellow spots reveal the area of spot analysis for pre-dentin (Pre). Scale bar 2 mm.

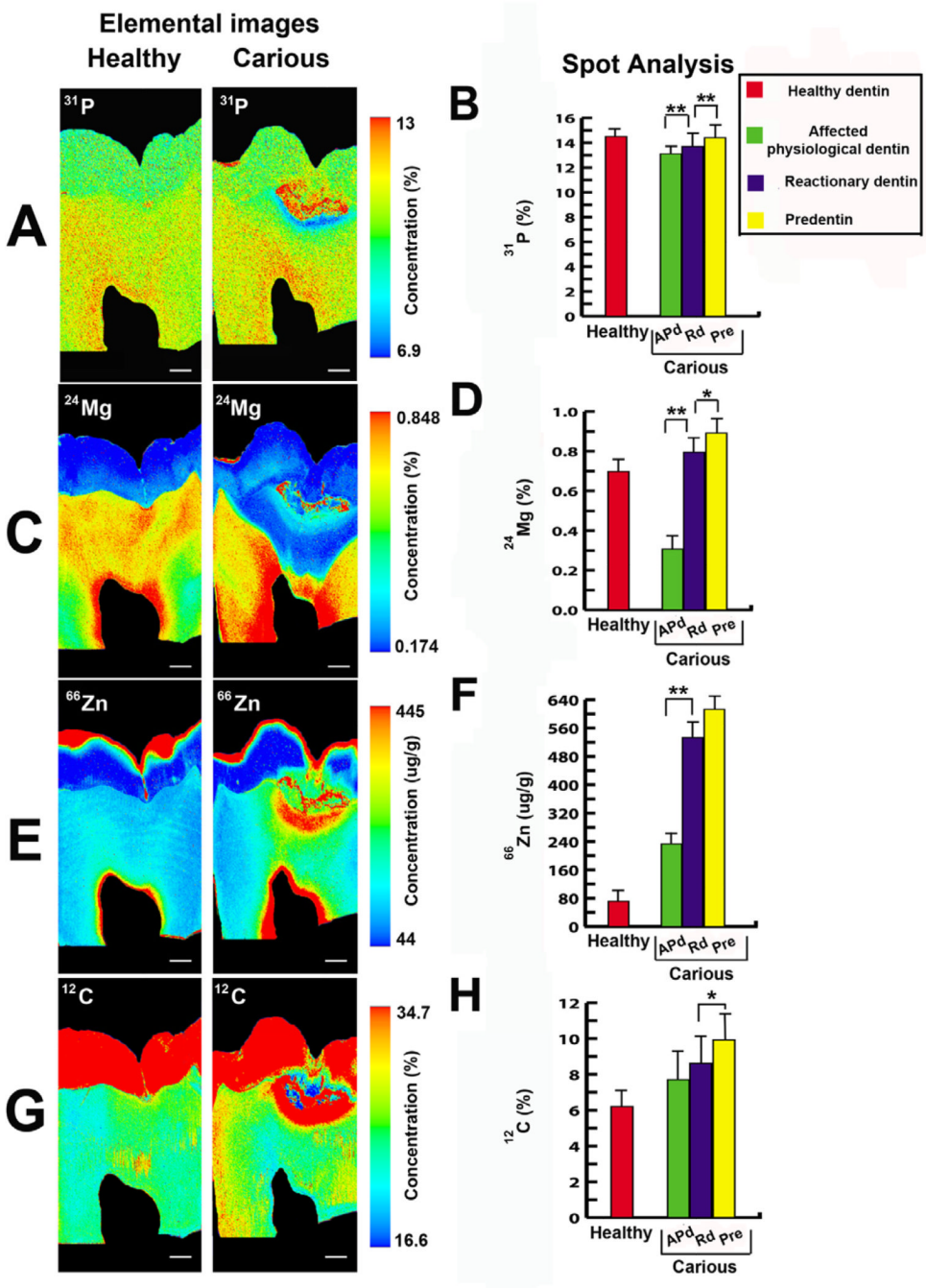

Figure 6. Representative elemental images (^{31}P, ^{24}Mg, ^{66}Zn and ^{12}C) of the areas analysed in healthy and carious samples in longitudinal section by LA-ICP-MS including physiological dentin (Pd), affected physiological dentin (APd), reactionary dentin (Rd) and pre-dentin (Pre)

The bar charts represent quantitative data (^{31}P, ^{24}Mg, ^{66}Zn and ^{12}C) for seven spot analysis of affected physiological dentin (APd), reactionary dentin (Rd) and pre-dentin (Pre) in carious samples and physiological dentin (Pd)in healthy samples. [^{31}P], [^{24}Mg] and [^{66}Zn] were significantly increased in Rd compared to APd. [^{31}P], [^{24}Mg] and [^{12}C] were significantly different between Rd and Pre. All values depict means ± SD. *P ≤ 0.05; ** P ≤ 0.02. (A) Elemental image of [^{31}P] in healthy (first panel) and carious (second panel) samples. In carious samples [^{31}P] gradually increased toward the pulp (n=3 teeth). Scale bar

2 mm. (B) The bar chart presents the significant increase of [^{31}P] in Rd compared to APd and increase in Pre compared to Rd (n=6 teeth). (C) Elemental mapping of the [^{24}Mg] gradient in healthy (first panel) and carious (second panel) samples. In carious samples, [^{24}Mg] decreased in APd under the carious lesion but increased in the area close to the pulp (n=3 teeth). Scale bar 2 mm. (D) The bar chart shows the marked increase of [^{24}Mg] in Rd compared to APd but gradual increase in Pre compared to Rd (n=6 teeth). (E) Elemental images of [^{66}Zn] in healthy (first panel) and carious (second panel) samples. In carious samples, APd under carious lesion shows intense [^{66}Zn] gradient but higher intensity of [^{66}Zn] was found close to the pulp (n=3 teeth). Scale bar 2 mm. (F) The bar chart reveals the significant increase of [^{66}Zn] in Rd compared to APd (n=6 teeth). (G) Elemental images of [^{12}C] in healthy (first panel) and carious (second panel) samples (n=3 teeth). Scale bar 2 mm. (H) The bar chart shows high variation of [^{12}C] in APd of carious sample. The difference was not significant between APd and Rd. However, the difference in [^{12}C] content in Pre and Rd was significant (n=6 teeth).

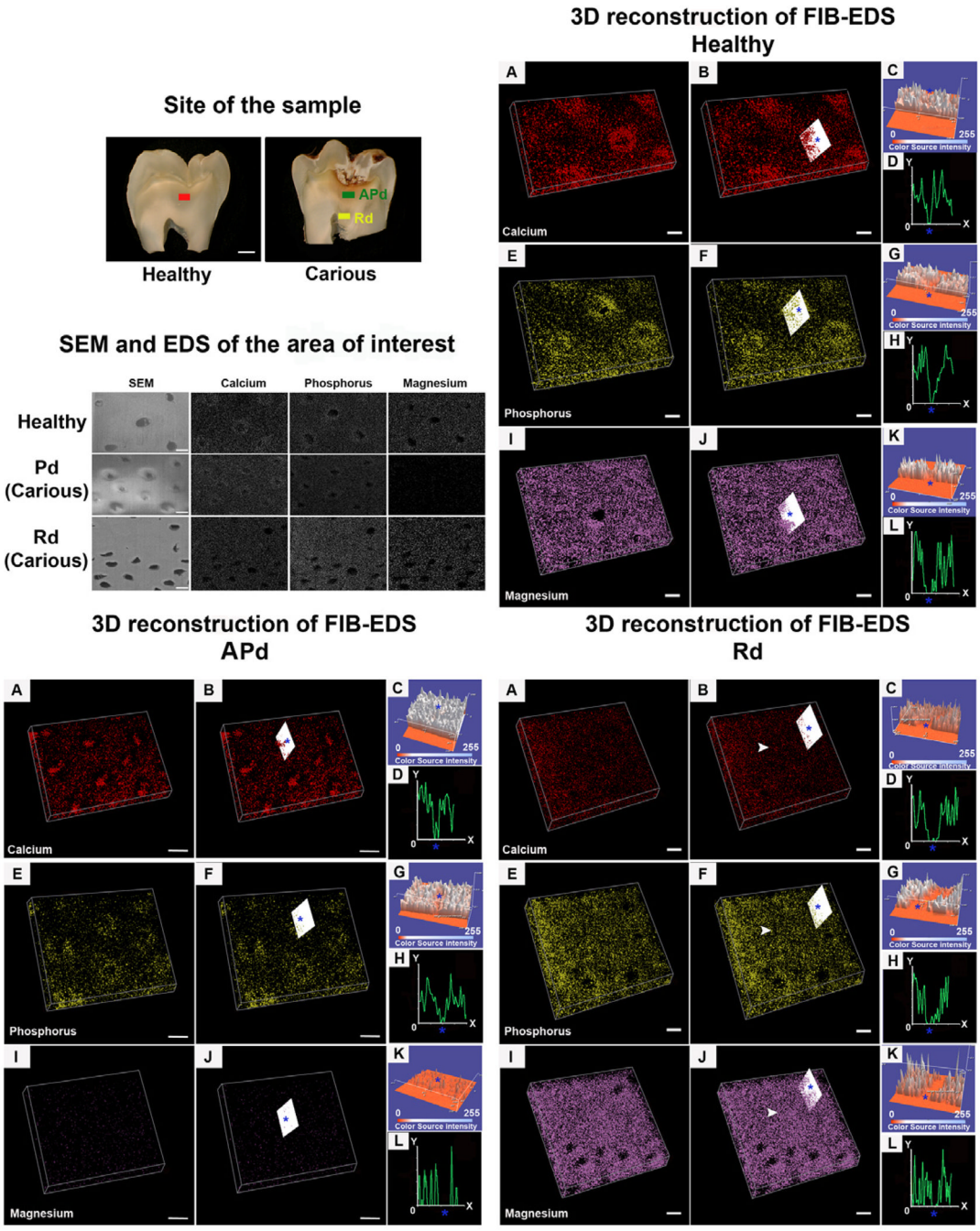

Figure 7. Representative images of the areas analysed and 3D reconstruction of the elements of interest (calcium, phosphorus and magnesium) in healthy and carious samples obtained by FIB-EDS analysis

Differences in distribution of elements of interest in each area including dentin in healthy sample, affected physiological dentin (APd) and reactionary dentin (Rd) in carious samples were found. The examples of the analysed sites from the samples are demonstrated in “Site of the sample”. The red bar is the analysed site from a healthy dentin sample, the green bar represents analysed site in APd and the yellow bar represents the analysed site in Rd from a carious sample. Scale bar 2 mm. The cross-sectional zones of sites of interest observed

under SEM and the example of a single slide EDS scan on those samples are exhibited in "SEM and EDS of area of interest". Scale bar 2 μm.

Healthy sample. (A) 3D reconstruction of calcium detected by FIB-EDS scanned from cross-sections of dentin. Scale bar 2 μm. (B) The slice analysed (white slice) shows accumulation of calcium around dentinal tubules (blue star) but dispersion of calcium in the inter-tubular area. Scale bar 2 μm. This was confirmed by surface plot (C) and plot profile (D). (E) 3D reconstruction of FIB-EDS scans of phosphorus from cross-sections of dentin. Scale bar 2 μm. (F) Accumulation of phosphorus around the dentinal tubules (blue star) was also observed (white slice). Scale bar 2 μm. This observation was confirmed by surface plot (G) and plot profile (H). (I) 3D reconstruction of magnesium in cross-sections. Scale bar 2 μm. (J) Similar distribution of magnesium around the tubules (blue star) and inter-tubular dentin was found. Scale bar 2 μm. Analyses from surface plots (K) and plot profiles (L) confirmed the observation (n=2 teeth).

Affected physiological dentin (APd) from carious sample. (A) 3D reconstruction of detected calcium from FIB-EDS of cross-sections of dentin. Scale bar 2 μm. (B) The analysis (white slice) reveals a calcium plug inside the tubule (blue star). No accumulation of calcium around the tubules was detected. Scale bar 2 μm. The observation was confirmed by surface plot (C) and plot profile (D). (E) 3D reconstruction of phosphorus detected by FIB-EDS scan from cross-sections of dentin. Scale bar 2 μm. (F) The accumulation of phosphorus around dentinal tubules (blue star) was observed. Lower intensity of phosphorus was recorded in inter-tubular dentin. Scale bar 2 μm. Confirmed by surface plot (G) and plot profile (H). (I) 3D reconstruction of magnesium in cross-sections of dentin. Magnesium had very weak signal in APd. Scale bar 2 μm. (J) The analysis (white slice) indicates the similarity of the distribution of magnesium in the area around dentinal tubules (blue star) and inter-tubular dentin. Scale bar 2 μm. This observation was confirmed by analysis of surface plots (K) and plot profiles (L) (n=2 teeth).

Reactionary dentin (Rd) from carious sample. (A) 3D reconstruction of calcium detected from FIB-EDS scans in cross-sections. Scale bar 2 μm. (B) The analysis (white slice) reveals the similarity of distribution of calcium between peritubular (blue star) and inter-tubular dentin. The same intensity of calcium signal was observed in areas devoid of tubules (white arrow). Scale bar 2 μm. This observation was confirmed by surface plots (C) and plot profiles (D). (E) 3D reconstruction of detected phosphorus from FIB-EDS scans from cross-sections of dentin. Scale bar 2 μm. (F) Phosphorus was also detected in areas devoid of tubules (white arrow). Phosphorus was similarity distributed in the peritubular (blue star) and inter-tubular dentin. Scale bar 2 μm. Findings were confirmed by surface plots (G) and plot profiles (H). (I) 3D reconstruction of magnesium in cross-sections of dentin. Scale bar 2 μm. (J) High intensity of magnesium was detected throughout Rd including area devoid of tubules (white arrow). Similarity intensitiy of magnesium signal was detected for peritubular (blue star) and inter-tubular dentin. Scale bar 2 μm. This was confirmed by surface plots (K) and plot profiles (L) (n=2 teeth).

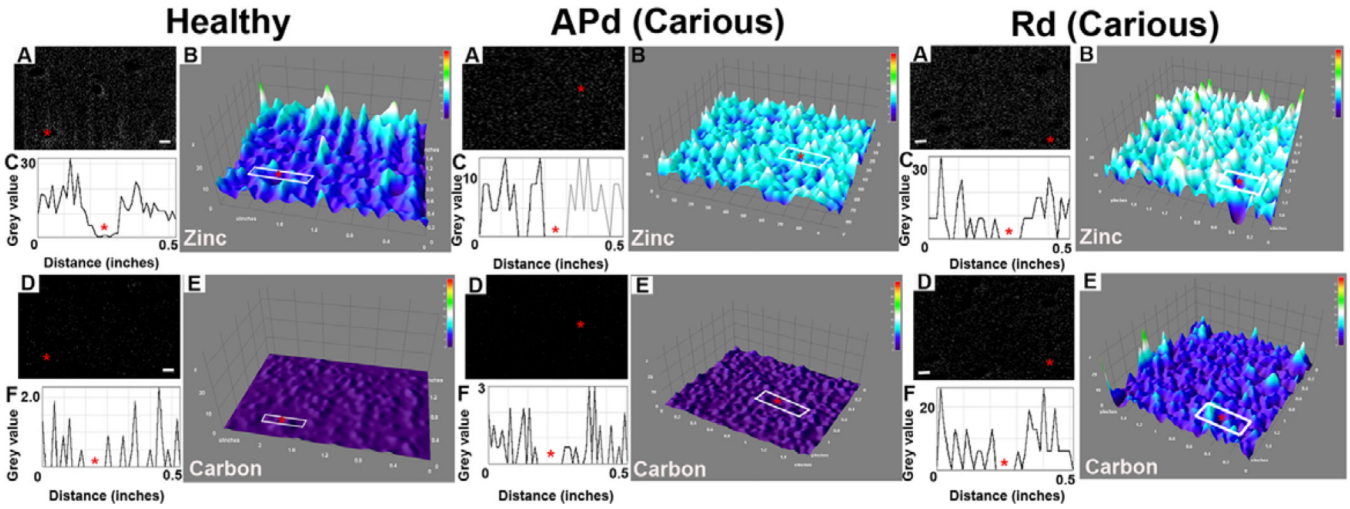

Figure 8. Representative images for zinc and carbon distribution detected by FIB-EDS from cross-sections of dentin

The different intensities and distribution of these elements in each area are displayed.

Healthy sample. (A) Representative image of FIB-EDS scan for zinc. Scale bar 2 μm. (B) 3D surface plot of FIB-EDS image of zinc presents a weak signal, with accumulation of zinc around the tubules (red star). (C) Plot profile of the area in white box in (B) confirms the accumulation of zinc around the tubule (red star). (D) Representative image of detected carbon from FIB-EDS scan. Scale bar 2 μm. (E) The 3D surface plot of carbon presents a weak signal with similar distribution between peritubular and inter-tubular dentin surrounding the tubule (red star). (F) The plot profile in white box (E) confirms the finding (n=2 teeth).

Affected physiological dentin (APd) from carious sample. (A) Representative image of zinc detected by FIB-EDS. Scale bar 2 μm. (B) 3D surface plot reveals the higher intensity of zinc compared to healthy sample. Accumulation of zinc around dentinal tubules (red star) was preserved. Confirmed by plot profiles (C). (D) Representative image of carbon detected by FIB-EDS. Scale bar 2 μm. (E) The 3D surface plot presents a weak signal for carbon in APd with dispersed distribution. (F) Plot profile of the area in white box (E) confirms this observation (n=2 teeth).

Reactionary dentin (Rd) from carious sample. (A) Representative image of detected zinc from FIB-EDS. Scale bar 2 μm. (B) The 3D surface plot shows higher intensity of zinc in Rd compared to healthy and APd but similar distribution of zinc was observed. (C) Plot profile in white box (B) confirms the finding. (D) Representative image of carbon detected from FIB-EDS. Scale bar 2 μm. (E) The 3D surface plot shows higher intensity of carbon in Rd compared to healthy dentin and APd. The similarity of distribution of carbon in the area around the tubule (red star) and inter-tubular dentin is apparent. (F) Plot profiles in white box (E) confirm the observation (n=2 teeth).

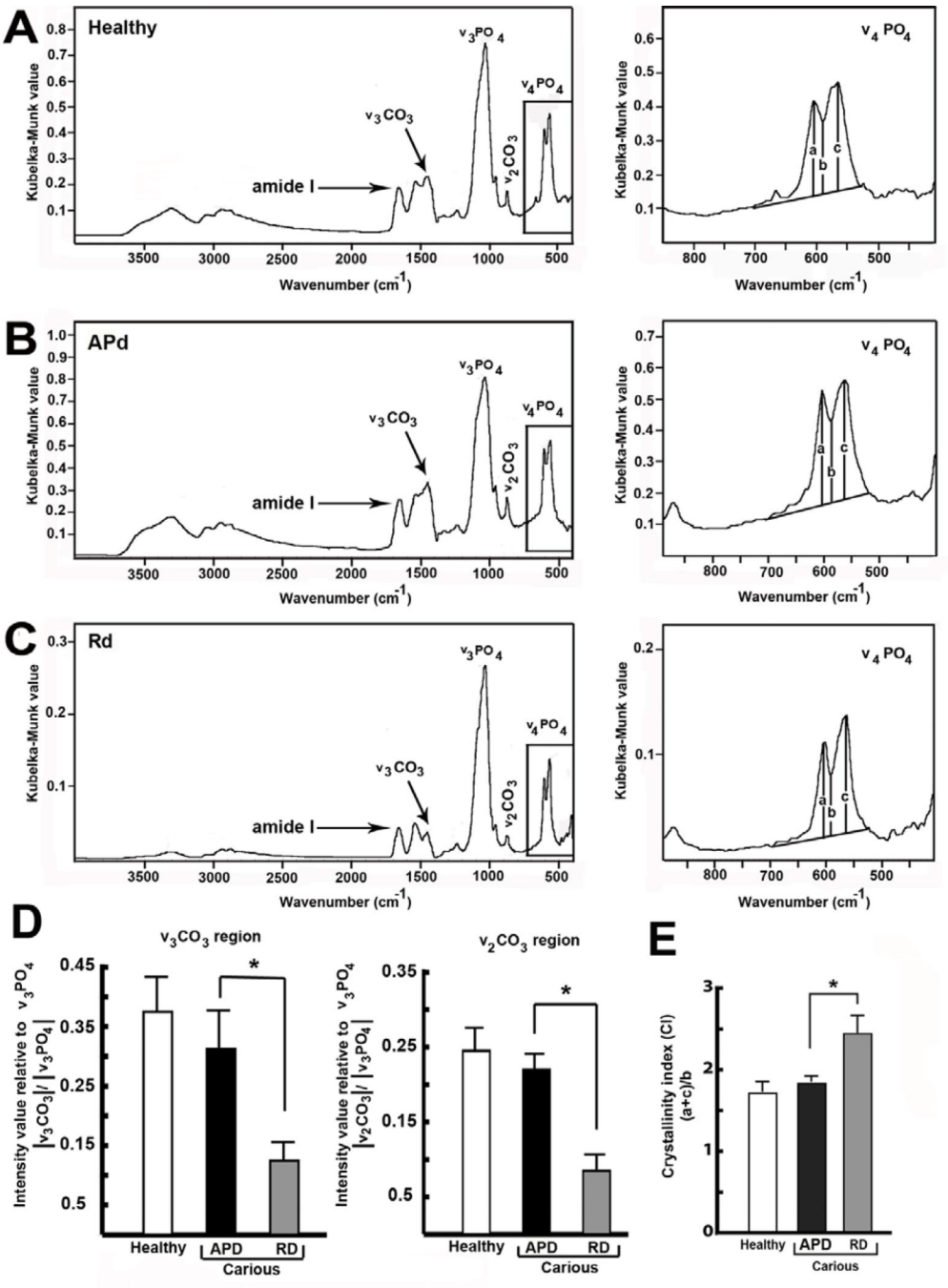

Figure 9. Diffuse reflectance infrared Fourier transform spectroscopy (DRIFTS) analysis of dentin powder

(A) DRIFTS absorbance spectrum of healthy dentin powder (first panel). Detailed DRIFTS absorbance spectrum of healthy dentin powder between 400 and 850 cm^{-1} (second panel). (B) DRIFTS absorbance spectrum of APd powder (first panel). Details DRIFTS absorbance spectrum of APd powder between 400 and 900 cm^{-1} (second panel). (C) DRIFTS absorbance spectrum of Rd powder (first panel) and the DRIFTS absorbance spectrum of Rd powder between 400 and 900 cm^{-1} (second panel). (D) Bar graph representing intensity value relative to anti-symmetric ν_3 PO_4 stretching mode in ν_3 CO_3^{2-} and ν_2 CO_3 regions (n=3 teeth). The B-type carbonate substitution in Rd is lower compared to healthy dentin

and APd in both regions. (E) Bar graph demonstrating Crystallinity Index (CI) produced by $(a+c)/b$. In Rd, CI is significantly higher compared to healthy dentin and APd (n=3 teeth). The data for DRIFTS analysis are expressed as mean values ± SD. * $p \leq 0.05$.

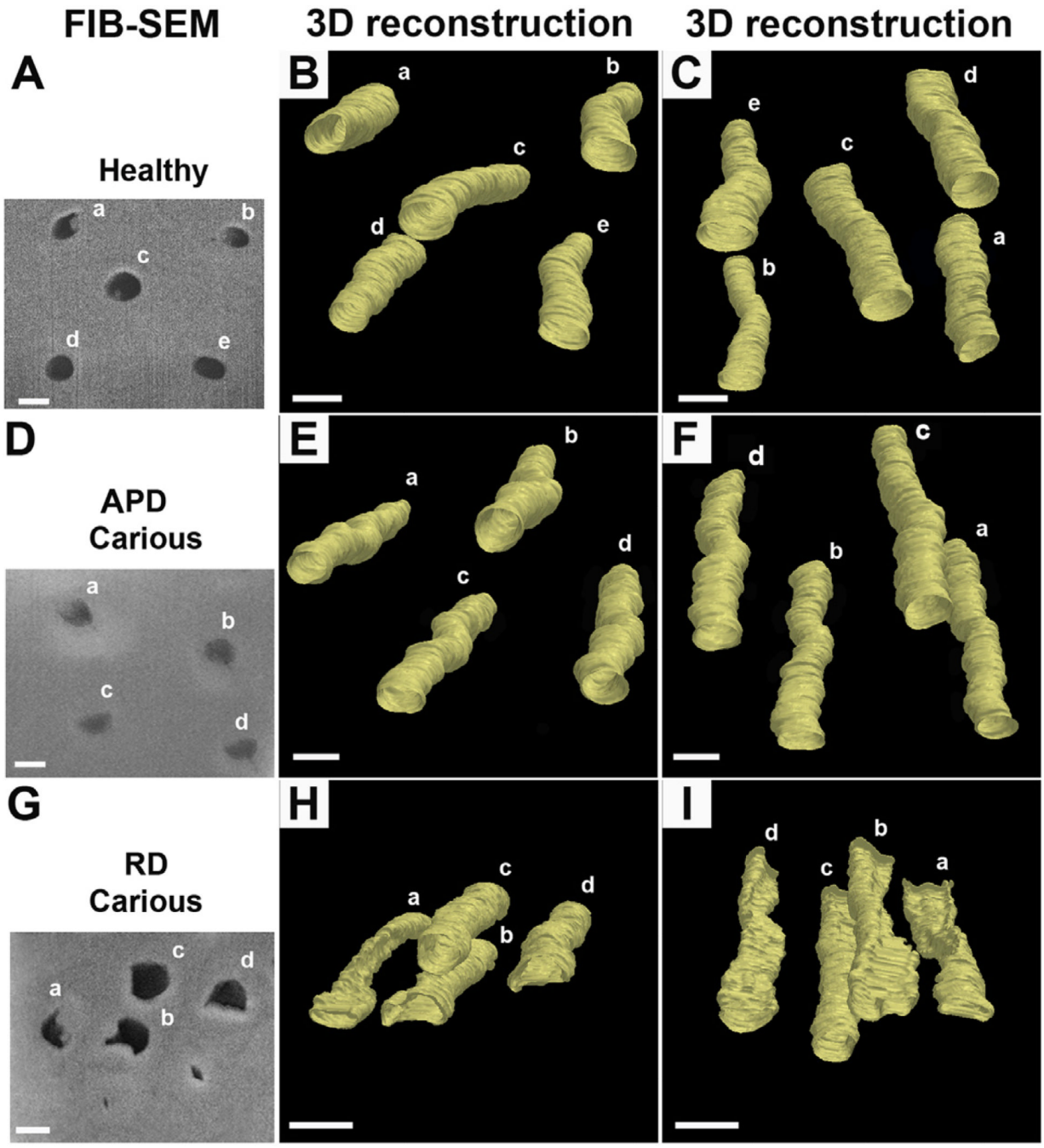

Figure 10. Representative images from 3D reconstruction of cross-sections of areas of interest using FIB-SEM

Difference in tubular structure of dentin in Rd compared with healthy dentin and APd, was observed. (A) Cross-section of analysed site in healthy sample observed under SEM. Scale bar 2 μm. (B) and (C) 3D reconstruction of tubular structure in healthy sample in different views. Uniformly round tubules were observed (n=40 tubules from 2 teeth). Scale bar 2 μm. (D) Scanning electron micrograph of a cross-section of APd in carious sample. Scale bar 2 μm. (E) and (F) different views of the 3D reconstruction of tubular structure in APd from carious sample. Round tubular structure as seen in healthy sample was observed (n=40 tubules from 2 teeth). Scale bar 2 μm. (G) Cross-section of Rd from carious sample observed

under SEM. The slit and irregular structures of dentinal tubules are evident. Scale bar 2 μm. (H) and (I) 3D reconstruction of tubular structure in Rd from carious sample in different views. Note the twisted appearance of the dentinal tubules in Rd (n=40 tubules from 2 teeth). Scale bar 2 μm.

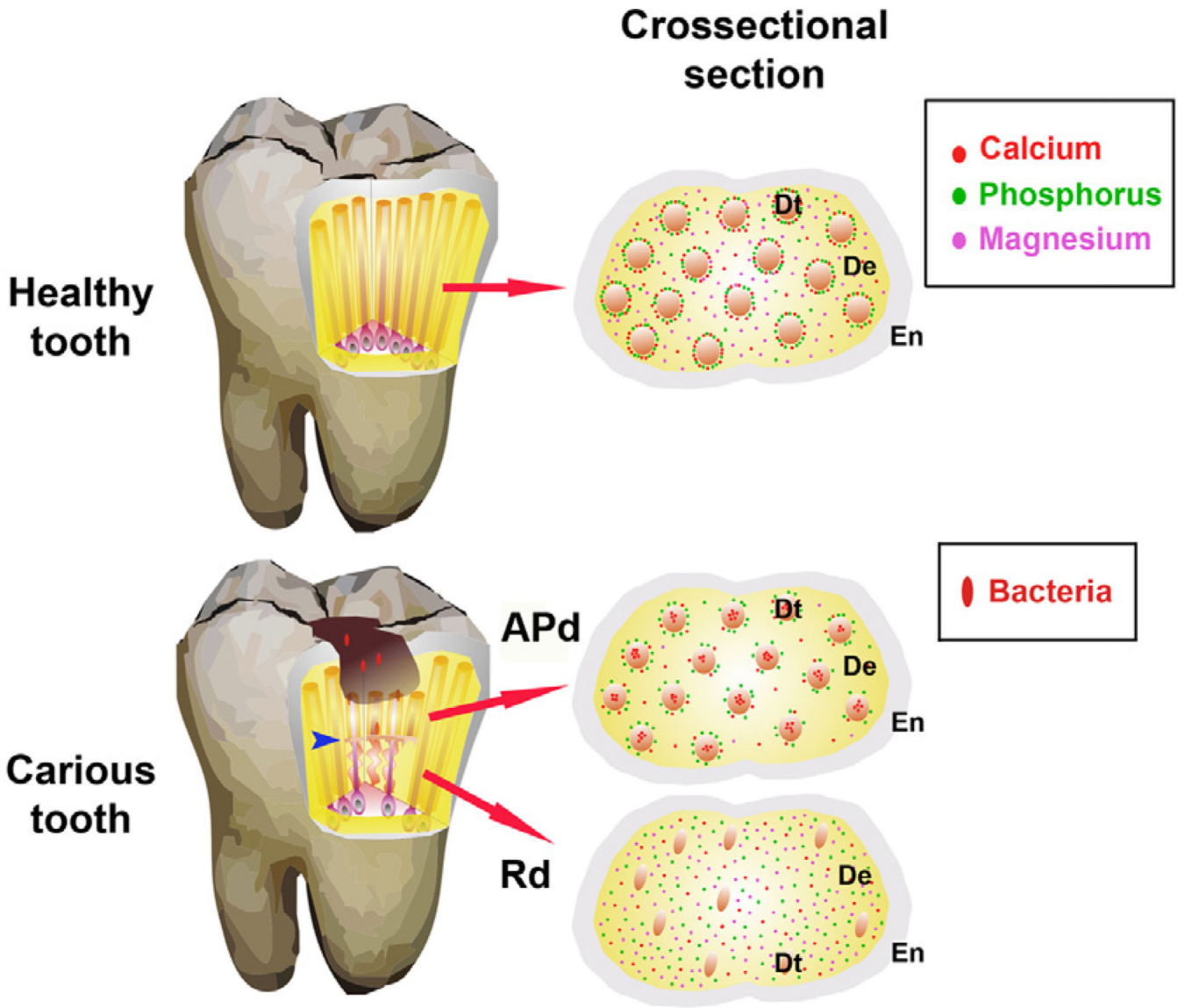

Figure 11. Diagrammatic representation of tooth structure affected by the carious Process

Healthy tooth. Cross-section shows the enamel (En), dentin (De) and dentinal tubules (Dt) with mineral content. A highly mineralised calcium and phosphorus annular ring surrounding each Dt is observed with dispersion of magnesium in peritubular and inter-tubular dentin. ***Carious tooth***. When bacterial invasion occurs calcium is lost from peritubular dentin and forms an intra-tubular plug. The phosphorus annular ring persists in affected physiological dentin (APd), but magnesium decreases. Reactionary dentin (Rd) formed in response to carious stimulation displays lower numbers of tubules and odontoblast processes. The cross-section shows reduction of diameter of tubules with scattered distribution of all elements but higher intensity of phosphorus and magnesium compared to dentin from healthy teeth and APd. The modified helical tubular structure in Rd (blue arrow) helps prevent the invasion of bacteria and potentially, acts as a shock absorber to compensate for the loss of upper tooth structure due to the carious lesion.